Spatial Distribution of the Milky Way Hot Gaseous Halo Constrained by *Suzaku* X-Ray Observations

Shinya Nakashima[1] , Yoshiyuki Inoue[2] , Noriko Yamasaki[3], Yoshiaki Sofue[4] , Jun Kataoka[5] , and Kazuhiro Sakai[6]

[1] RIKEN High Energy Astrophysics Laboratory, 2-1 Hirosawa, Wako, Saitama, 351-0198, Japan; shinya.nakashima@riken.jp
[2] RIKEN Interdisciplinary Theoretical and Mathematical Sciences (iTHEMS) Program, 2-1 Hirosawa, Wako, Saitama, 351-0198, Japan
[3] Institute of Space and Astronautical Science, Japan Aerospace Exploration Agency, 3-1-1 Yoshinodai, Chuo-ku, Sagamihara, Kanagawa 252–5210, Japan
[4] Institute of Astronomy, The University of Tokyo, Mitaka, Tokyo 181-0015, Japan
[5] Research Institute for Science and Engineering, Waseda University, 3-4-1 Okubo, Shinjuku, Tokyo 169-8555, Japan
[6] NASA Goddard Space Flight Center, Code 662, Greenbelt, MD 20771, USA
Received 2018 May 2; revised 2018 June 12; accepted 2018 June 12; published 2018 July 20

Abstract

The formation mechanism of the hot gaseous halo associated with the Milky Way is still under debate. We report new observational constraints on the gaseous halo using 107 lines of sight of the *Suzaku* X-ray observations at $75° < l < 285°$ and $|b| > 15°$ with a total exposure of 6.4 Ms. The gaseous halo spectra are represented by a single-temperature plasma model in collisional ionization equilibrium. The median temperature of the observed fields is 0.26 keV (3.0×10^6 K) with a typical fluctuation of ∼30%. The emission measure varies by an order of magnitude and marginally correlates with the Galactic latitude. Despite the large scatter of the data, the emission measure distribution is roughly reproduced by a disk-like density distribution with a scale length of ∼7 kpc, a scale height of ∼2 kpc, and a total mass of ∼$5 \times 10^7 M_\odot$. In addition, we found that a spherical hot gas with the β-model profile hardly contributes to the observed X-rays but that its total mass might reach $\gtrsim 10^9 M_\odot$. Combined with indirect evidence of an extended gaseous halo from other observations, the hot gaseous halo likely consists of a dense disk-like component and a rarefied spherical component; the X-ray emissions primarily come from the former, but the mass is dominated by the latter. The disk-like component likely originates from stellar feedback in the Galactic disk due to the low scale height and the large scatter of the emission measures. The median [O/Fe] of ∼0.25 shows the contribution of the core-collapse supernovae and supports the stellar feedback origin.

Key words: Galaxy: halo – ISM: structure – X-rays: ISM

Supporting material: machine-readable table

1. Introduction

The evolution of galaxies is regulated by inflowing gas from the intergalactic medium and outflowing gas from the disk region (Tumlinson et al. 2017, and references therein). In a spiral galaxy with a mass of $\gtrsim 10^{12} M_\odot$, inflowing gas is expected to form a hot gaseous halo ($T > 10^6$ K) via accretion shocks and adiabatic compression extending to the viral radius (Kereš et al. 2009; Crain et al. 2010; Joung et al. 2012), while stellar feedback forms superbubbles in the disk and drives multiphase gas outflows up to several kiloparsecs above the disk (Hill et al. 2012; Kim & Ostriker 2018). Numerical simulations show divergent behavior in the formation of gaseous halos owing to different implementations of feedback and star formation (Stewart et al. 2017). Therefore, observational constraints on the properties of hot gaseous halos are essential to understanding the amount of accreting and outflowing gas.

A hot gaseous halo around the Milky Way (hereafter MW) has been confirmed via X-ray observations. Early X-ray missions found a diffuse X-ray background in the 0.5–1.0 keV band (Tanaka & Bleeker 1977; McCammon & Sanders 1990, and references therein), and the *ROSAT* all-sky survey revealed the detailed spatial distribution of the X-ray emissions (Snowden et al. 1997); in addition to the prominent features around the center of the MW, significant excesses that cannot be explained by the superposition of extragalactic active galactic nuclei are found. After the advent of grating spectrometers and microcalorimeters, absorption and emission lines of

O VII and O VIII at zero redshift were observed, which provide evidence of the association of hot gas with the MW (e.g., Fang et al. 2002; McCammon et al. 2002).

The detailed spatial distribution of the MW hot gaseous halo has been extensively investigated using emission and absorption lines over the past decade. Combined with emission- and absorption-line measurements toward LMC X-3, Yao et al. (2009) constructed a disk-like distribution model with a scale height of a few kiloparsecs, suggesting a significant contribution of hot gas produced by stellar feedback rather than accretion shocks. Similar results were obtained in other two lines of sight (Hagihara et al. 2010; Sakai et al. 2014). Conversely, Gupta et al. (2012) presented a hot gas distribution extending up to ∼100 kpc using absorption-line data toward several extragalactic sources. Miller & Bregman (2013, 2015) analyzed measurements of 29 absorption lines and 649 emission lines and formulated an extended spherical morphology represented by the β model. The cause of the discrepancy between these results is not clear but might be due to different assumptions, such as the temperature profile and metallicity.

As a complement to the above line data analyses, broadband X-ray spectroscopy including the continuum has been performed. In contrast to the line data analyses, where temperature and metallicity need to be assumed, broadband spectroscopy can self-consistently determine the temperature, emission measure, and metallicity. This approach has been widely used for observations of nearby dark clouds with CCD detectors (Galeazzi et al. 2007; Henley et al. 2007, 2015a; Smith et al. 2007). However, systematic analyses with large

samples are limited owing to limited photon statistics compared to line measurements. Yoshino et al. (2009) analyzed 13 lines of sight of the *Suzaku* observations, and Henley & Shelton (2013) analyzed 110 lines of sight of the *XMM-Newton* observations.

In this paper, we present new broadband spectroscopic results of the MW hot gaseous halo using 107 lines of sight of the *Suzaku* observations. The X-ray CCDs aboard *Suzaku* (XIS; Koyama et al. 2007) have low and stable instrumental background and good spectral responses below 1 keV compared to the X-ray CCDs aboard *Chandra* and *XMM-Newton* (Mitsuda et al. 2007). Therefore, it is suitable for the spectroscopy of faint diffuse emission. The data selection and screening are explained in Section 2. The spectral modeling and results are shown in Section 3, and the interpretations of the results are discussed in Section 4.

2. Observations and Data Reduction

2.1. Data Selection from the Suzaku Archive

We used archival data of the *Suzaku*/XIS, which is sensitive to 0.2–12.0 keV X-rays. The XIS consists of three front-illuminated (FI) type CCDs (XIS0, XIS2, and XIS3) and one back-illuminated (BI) type CCD (XIS1) located at the focal planes of four independent X-ray telescopes (Serlemitsos et al. 2007). XIS2 has not been functioning since 2006 November and was not used in our analysis. The effective area at 1.5 keV is $\sim$1030 cm^2 combined with the remaining three sensors. The field of view (FOV) is $\sim$18′ × 18′ with a spatial resolution of $\sim$2′ in a half-power diameter.

We accumulated the observations pointing to the Galactic anticenter ($75° < l < 285°$) and outside the Galactic plane ($|b| > 15°$). Observations toward the Galactic center were not used because additional diffuse hot gas associated with past Galactic center activities would contaminate the results for the hot gaseous halo (e.g., Su et al. 2010; Kataoka et al. 2013; Nakashima et al. 2013; Miller & Bregman 2016).

The observations contaminated by other X-ray-emitting extended objects such as clusters of galaxies, galaxies, supernova remnants, and superbubbles were excluded. Bright compact objects are other contaminant sources owing to the wide point-spread functions of the *Suzaku* telescopes. Referring to the HEASARC Master X-ray Catalog,[7] we removed observations aimed at sources brighter than 10^{11} erg s cm^{-2}. Photons from extremely bright sources outside the XIS FOV are also scattered into the detector, that is, so-called "stray light" (Serlemitsos et al. 2007). Therefore, observations within a 90′ radius of sources of $F_X > 10^{10}$ erg s cm^{-2} were discarded. In addition, the observations of specific targets, such as the Moon, Jupiter, nearby dark clouds (MBM 16, MBM 20, and LDN 1563), and a helium focusing cone, were excluded. Finally, observations of which effective exposures were less then 10 ks after the screening described in the next section were also excluded. As a result of these selections, we accumulated 122 observations with a total exposure of $\sim$6.4 Ms (Figure 1 and Table 1). Some observations cover the same sky regions. To identify line-of-sight directions, we assigned the region IDs; the same region ID was assigned to the observations of the same sky region. The total number of lines of sight is 107.

2.2. Data Reduction

The selected XIS data were reprocessed via the standard pipeline with HEASOFT version 6.22 and the calibration database as of 2016 April 1. We then removed additional flickering pixels that were found in the long-term background monitoring.[8] Due to the charge leakage, segment A of the XIS0 was not used for the data taken after 2009 June 27.[9]

To remove point sources in the XIS FOVs, we created 0.7–5.0 keV raw count images where data from all the sensors were co-added and searched for source candidates using the `wavdetect` tool in the CIAO package.[10] Figure 2 shows an example of the results. We found 13 candidates in that image, including possible false detections, with a significance of $<3\sigma$. The number of detected sources in one observation ranged between 1 and 16, depending on the effective exposure times. All the detected candidates from the event list were removed via circular regions (Figure 2).

The geocoronal solar wind charge exchange (SWCX) emission is a possible contaminant source below 1 keV. Its flux varies on a timescale of hours and correlates with the proton flux of the solar wind (e.g., Fujimoto et al. 2007; Ishikawa et al. 2013). Previous studies have successfully reduced geocoronal SWCX contamination by screening out durations where the solar wind proton flux exceeds 4×10^8 protons cm^{-2} s^{-1} (e.g., Yoshino et al. 2009; Henley & Shelton 2013; Miller & Bregman 2015). We followed these screening criteria with the proton flux calculated from the OMNI database.[11]

For the data below 0.7 keV, we adopted one additional screening criterion to suppress contamination by the O I Kα emission from the sunlit Earth atmosphere. As reported by Sekiya et al. (2014), the O I Kα contamination has become significant since 2011 even after excluding periods where the angle between the satellite pointing direction and the sunlit Earth's rim (DYE_ELV) is less than 20°. This phenomenon is likely due to increasing solar activity. The O I Kα contamination can be reduced by applying a higher DYE_ELV threshold. Therefore, we used a new DYE_ELV threshold for individual observations; we calculated the 0.5–0.6 keV count rates for each DYE_ELV with a binning of 10° and determined the DYE_ELV threshold where the count rate significantly increases. The actual values are listed in Table 1. The standard screening criterion (DYE_ELV > 20°) is still applicable to some observations.

We extracted spectra from 0.4–0.7 keV and 0.7–5.0 keV separately; the day-Earth screening was only applied to the former spectra. Spectra of the FI CCDs (XIS0 and XIS3) were co-added to increase the photon statistics. The instrumental backgrounds were estimated from the night-Earth database using `xisnxbgen` (Tawa et al. 2008). Energy responses of each sensor were generated by `xisrmfgen` and `xissimarfgen` (Ishisaki et al. 2007).

3. Analysis and Results

We constructed a spectral model (Section 3.1) and fitted it to the data to derive the parameters of the hot gaseous halo

---

7   https://heasarc.gsfc.nasa.gov/W3Browse/all/xray.html

8   http://www.astro.isas.ac.jp/suzaku/analysis/xis/nxb_new2/

9   http://www.astro.isas.ac.jp/suzaku/analysis/xis/xis0_area_discriminaion/

10   http://cxc.harvard.edu/ciao/
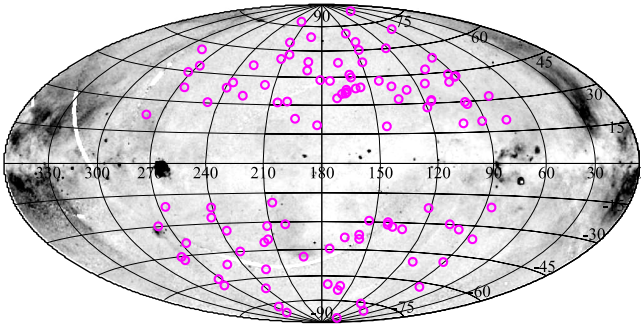
11   http://omniweb.gsfc.nasa.gov/ow.html

Figure 1. Directions of the 107 fields analyzed in this paper overlaid on a grayscale image of the *ROSAT* R45 band. The fields are located at $75° < l < 285°$ and $|b| > 15°$. The size of the circles is artificial, and the actual *Suzaku* FOV is $17'.8 \times 17'.8$.

(Section 3.2). Correlations between the parameters were also investigated (Section 3.3).

3.1. Spectral Model

Our spectral model consisted of three components: the hot gaseous halo, the local emission component, and the cosmic X-ray background (CXB). This model is similar to those used in previous broadband spectroscopy of the soft X-ray background (e.g., Henley & Shelton 2013), but it included recent updates of the atomic database, the solar metallicity, and the Galactic hydrogen column density as described below.

The hot gaseous halo component is described by a single-temperature plasma in collisional ionization equilibrium (CIE). We used the APEC plasma spectral model (Foster et al. 2012) with AtomDB version 3.0.9. The latest solar abundance table of Lodders et al. (2009) was adopted as a reference of the metallicity. In the spectral fitting, the plasma temperature (kT_{halo}) and the emission measure (EM$_{halo}$) were treated as free parameters. The metallicity is difficult to determine in a CCD spectrum because lines and radiative recombination continua from oxygen and iron exceed bremsstrahlung from hydrogen in $kT = 0.2$ keV plasma. Therefore, we allowed only the iron abundance (Z_{Fe}) to vary and fixed the other metal abundances to the solar values. The setting allowed us to obtain the abundance ratio of oxygen to iron ([O/Fe]$_{halo}$ = log$_{10}(Z_O/Z_{Fe})$). When Z_{Fe} was not constrained within 0.1–10 times the solar value during the fitting procedure, we fixed it to the solar value. Previously, several studies have assumed a metallicity of 0.3 solar instead of the solar value for the hot gaseous halo (e.g., Miller & Bregman 2015). We confirmed that fixing the abundances (except iron) to 0.3 solar increases EM$_{halo}$ by a factor of 3 without affecting the other parameters.

The local emission originates from the local hot bubble and the heliospheric SWCX (e.g., Fujimoto et al. 2007; Liu et al. 2017). Despite their debatable physical properties, a spectrum is empirically described by a single CIE plasma of $kT \sim 0.1$ keV with the solar metallicity in the CCD spectra (e.g., Smith et al. 2007; Yoshino et al. 2009; Henley & Shelton 2013). We used the same phenomenological model; the temperature was fixed to 0.1 keV, and the emission measure (EM$_{local}$) was allowed to vary.

The CXB is a superposition of unresolved extragalactic sources. An absorbed power-law function with a photon index of 1.45 represents the CXB spectrum in the 0.3–7 keV band (Cappelluti et al. 2017). The normalization of the power-law function at 1 keV (N_{CXB}) is $\sim$10 photons cm^{-2} s^{-1} sr^{-1} keV^{-1}

but spatially fluctuates by $\sim$15% for the XIS FOV ($\sim$0.8 deg^2) owing to the cosmic variance (Moretti et al. 2009). Therefore, we treated N_{CXB} as a free parameter in our spectral model.

The hot gaseous halo emission and the CXB are subject to absorption due to the Galactic cold interstellar medium. This absorption was modeled using TBabs code version 2.3 (Wilms et al. 2000), in which cross sections of dust grains and molecules are taken into account. The absorption hydrogen column density (N_H) of each line of sight was fixed to the value estimated by Willingale et al. (2013), in which the contributions of not only neutral hydrogen atoms ($N_{H\,I}$) but also molecular hydrogen (N_{H_2}) were included. We confirmed that using only the $N_{H\,I}$ values from Kalberla et al. (2005), which have been widely used in previous studies, has no significant impact on our results.

3.2. Spectral Fitting Results

Spectral fitting was performed with Xspec version 12.9.1n. Spectra in the same region IDs were simultaneously fitted. The best-fit parameters were determined by minimizing the *C*-statistic (Cash 1979) with a Poisson background.[12] To compensate for the systematic differences in the effective areas among the sensors (Tsujimoto et al. 2011), we allowed the relative normalization to vary between the BI and FI spectra.

Figure 3 shows an example of the fitting results. The local emission (blue curve) dominates the spectrum below 0.6 keV, whereas the CXB (purple curve) dominates the spectrum above 1.2 keV. The hot gaseous halo emission (red curves) fills the remaining excess in the range of 0.6–1.0 keV. The derived halo parameters, $kT_{halo} = 0.28$ keV and [O/Fe]$_{halo} = 0.40$, are primarily constrained by the emission lines of O VII, O VIII, Fe XVII, and Ne IX. Table 1 summarizes the best-fit parameters for all the regions.

A histogram of the best-fit kT_{halo} is shown in the left panel of Figure 4. The median is 0.26 keV, and the 16th–84th percentile range is 0.19–0.32 keV. The shape of the distribution is nearly symmetric with respect to the median value; however, six regions show significantly high temperatures ($kT > 0.4$ keV). Spectra of these high-temperature regions are shown in Figure 5. They exhibit an excess of Fe L-shell lines between 0.7 and 0.9 keV and no clear O VIII Lyα line. That is because the best-fit temperatures of these regions are higher than those of other regions. The lack of an O VIII Lyα line is not caused by interstellar absorption because the transmission of O VIII Lyα is >50% for those regions, where N_H is in the range of $(1.3–10.3) \times 10^{20}$ cm^{-2}.

The middle and the right panels of Figure 4 show kT_{halo} versus $|l|$ and $|b|$, respectively, where $|l|$ is defined as

$$|l| = \begin{cases} l & (0° \leqslant l < 180°) \\ 360° - l & (180° \leqslant l < 360°). \end{cases} \quad (1)$$

Spearman rank correlations for those two plots are shown in Table 2. We found a marginal negative correlation of $\rho = -0.24$ between kT_{halo} and $|b|$ with a *p*-value of 0.019. Conversely, no correlation was observed between kT_{halo} and $|l|$.

Figure 6 is the same as Figure 4, but for EM$_{halo}$. The histogram of EM$_{halo}$ is spread over more than one order of magnitude; the minimum is 0.6×10^{-3} cm^{-6} pc, the

---

[12] Referred to as the "W-statistics" in the Xspec manual (https://heasarc.nasa.gov/xanadu/xspec/manual/XSappendixStatistics.html).

Table 1
Observations and Fitting Results

Region (1)	Sequence (2)	Target Name (3)	l (4)	b (5)	t (6)	DYE (7)	N_H (8)	kT_{halo} (9)	EM_{halo} (10)	$[O/Fe]_{halo}$ (11)	Z_{halo} (12)	S_{halo} (13)	kT_{local} (14)	EM_{local} (15)	Z_{local} (16)	N_{CXB} (17)	C/dof (18)
1	802083010	COMABKG	75.73	83.17	21.7	>20	1.0	$0.19^{+0.16}_{-0.01}$	$0.6^{+0.4}_{-0.4}$	<0.92	1	0.7	0.1	$25.3^{+3.3}_{-4.3}$	1	$8.0^{+0.4}_{-0.3}$	2858.7/2518
2	403008010	AM HERCULES BGD	77.40	20.28	44.3	>20	6.5	$0.29^{+0.03}_{-0.03}$	$3.1^{+0.4}_{-0.4}$	>−0.03	1	2.4	0.1	$18.2^{+2.0}_{-2.0}$	1	$9.8^{+0.3}_{-0.3}$	2636.1/2518
3	704008010	1739+518	79.53	31.85	16.9	>20	3.1	$0.30^{+0.03}_{-0.03}$	$4.7^{+0.7}_{-0.6}$	>0.01	1	3.7	0.1	$26.8^{+4.0}_{-3.9}$	1	$10.0^{+0.5}_{-0.5}$	2819.8/2518
4	406007010	1FGL J2339.7−0531	81.35	−62.47	89.0	>20	3.2	$0.15^{+0.02}_{-0.00}$	$7.8^{+0.5}_{-2.4}$	<−0.20	1	3.9	0.1	$6.4^{+5.1}_{-2.4}$	1	$9.9^{+0.2}_{-0.1}$	2743.7/2518
5	707009010	2FGL J0022.2−1853	82.15	−79.37	32.6	>30	2.1	$0.30^{+0.05}_{-0.03}$	$2.3^{+0.5}_{-0.5}$	>−1.00	1	2.0	0.1	<29.4	1	$11.9^{+0.4}_{-0.4}$	2702.8/2518
6	709004010	SWIFT J2248.8+1725	85.73	−36.41	13.1	>90	7.7	$0.22^{+0.01}_{-0.01}$	$5.9^{+3.0}_{-0.8}$	$−0.04^{+0.58}_{-0.25}$	1	4.9	0.1	<27.0	1	$10.4^{+0.2}_{-0.2}$	2658.3/2518
7	502047010	LOW_LATITUDE_86-21	86.00	−20.79	81.6	>20	7.9	$0.28^{+0.01}_{-0.01}$	$5.1^{+0.3}_{-0.3}$	$0.40^{+0.13}_{-0.07}$	1	4.2	0.1	$20.7^{+1.3}_{-1.3}$	1	$9.7^{+0.2}_{-0.2}$	2537.7/2518
8	704050010	SDSS J1352+4239	88.11	70.10	21.3	>20	1.0	$0.22^{+0.05}_{-0.03}$	$2.3^{+0.9}_{-0.7}$	>−0.96	1	1.7	0.1	<30.7	1	$10.3^{+0.4}_{-0.4}$	2961.5/2518
9	501005010	DRACO HVC REGION B	90.08	42.68	61.6	>20	1.5	$0.18^{+0.02}_{-0.01}$	$3.3^{+0.8}_{-0.8}$	<0.31	1	2.3	0.1	$14.4^{+3.0}_{-2.9}$	1	$10.8^{+0.3}_{-0.2}$	2738.3/2518
10	708023010	MRK 533	90.63	−48.79	45.9	>50	5.2	$0.31^{+0.02}_{-0.02}$	$3.6^{+0.4}_{-0.4}$	$0.37^{+0.13}_{-0.10}$	1	3.1	0.1	$27.1^{+2.1}_{-2.1}$	1	$10.6^{+0.3}_{-0.3}$	2809.9/2518
11	501004010	DRACO HVC REGION A	91.21	42.38	61.2	>20	1.8	$0.24^{+0.03}_{-0.03}$	$1.8^{+0.3}_{-0.3}$	$0.11^{+0.60}_{-0.29}$	1	1.5	0.1	$21.1^{+1.8}_{-1.8}$	1	$11.4^{+0.3}_{-0.3}$	2675.4/2518
12	904001010	GRB 090709A	91.79	20.21	37.1	>20	8.5	$0.31^{+0.03}_{-0.03}$	$3.6^{+0.6}_{-0.6}$	>−0.12	1	3.0	0.1	$15.3^{+2.4}_{-2.4}$	1	$12.4^{+0.4}_{-0.4}$	2877.9/2518
13	707008010	2FGL J1502.1+5548	92.73	52.90	23.5	>30	1.4	$0.14^{+0.04}_{-0.00}$	$9.8^{+2.4}_{-6.3}$	<0.76	1	4.1	0.1	<38.8	1	$10.1^{+0.3}_{-0.3}$	2737.5/2518
14	501101010	DRACO ENHANCEMENT	93.99	43.99	33.8	>20	1.1	$0.38^{+0.04}_{-0.04}$	$2.8^{+0.4}_{-0.4}$	>0.22	1	2.2	0.1	$23.1^{+2.0}_{-1.9}$	1	$9.6^{+0.4}_{-0.4}$	2661.1/2518
15	708026010	NGC 235A	94.13	−85.92	13.2	>60	1.5	$0.26^{+0.08}_{-0.07}$	$1.5^{+0.9}_{-0.6}$	0.0 (fixed)	1	1.4	0.1	$24.9^{+3.9}_{-4.6}$	1	$9.4^{+0.4}_{-0.4}$	2849.5/2519
16	100018010	NEP	95.75	28.68	88.4	>20	4.0	$0.20^{+0.00}_{-0.00}$	$9.0^{+0.6}_{-0.6}$	$0.26^{+0.11}_{-0.10}$	1	6.1	0.1	$13.4^{+1.6}_{-1.5}$	1	$11.9^{+0.2}_{-0.2}$	5540.1/5040
...	500026010	NEP	95.79	28.66	26.4	>20	4.0	...	...	...	...	...	...	...	...	...	...
17	504070010	NEP #1	96.38	29.79	50.0	>30	4.5	$0.27^{+0.01}_{-0.02}$	$1.9^{+0.3}_{-0.2}$	$0.25^{+0.16}_{-0.12}$	1	1.6	0.1	$15.9^{+1.0}_{-1.4}$	1	$8.5^{+0.2}_{-0.2}$	10781.8/ 10084
...	504072010	NEP #2	96.39	29.79	47.7	>20	4.5	...	...	...	...	...	...	...	...	...	...
...	504074010	NEP #3	96.39	29.79	42.5	>20	4.5	...	...	...	...	...	...	...	...	...	...
...	504076010	NEP #4	96.40	29.79	49.8	>20	4.5	...	...	...	...	...	...	...	...	...	...
18	100030020	A2218_offset	97.72	40.12	46.2	>20	2.4	$0.24^{+0.04}_{-0.03}$	$1.5^{+0.3}_{-0.3}$	>−0.45	1	1.1	0.1	$15.3^{+1.4}_{-1.4}$	1	$10.5^{+0.3}_{-0.3}$	2552.1/2518
19	408030010	SWIFT J2319.4+2619	98.48	−32.22	20.0	>60	6.8	$0.16^{+0.02}_{-0.02}$	$12.5^{+3.2}_{-2.6}$	<−0.15	1	6.6	0.1	<36.6	1	$10.8^{+0.4}_{-0.4}$	2848.0/2518
20	705027010	EMS1341	102.86	19.44	14.1	>20	21.0	$0.31^{+0.04}_{-0.03}$	$5.6^{+1.2}_{-1.2}$	>−0.32	1	4.9	0.1	<13.9	1	$10.6^{+0.6}_{-0.6}$	2778.4/2518
21	704014010	UGC 12741	105.66	−29.88	48.0	>20	7.9	$0.24^{+0.03}_{-0.03}$	$3.2^{+0.6}_{-0.6}$	<0.28	1	3.1	0.1	<15.8	1	$9.8^{+0.3}_{-0.3}$	2838.8/2518
22	705023010	LEDA 84274	106.76	47.40	49.5	>20	1.3	$0.71^{+0.05}_{-0.06}$	$2.0^{+0.5}_{-0.5}$	$0.36^{+0.23}_{-0.14}$	1	2.2	0.1	$18.4^{+1.8}_{-1.8}$	1	$9.6^{+0.3}_{-0.3}$	2758.0/2518
23	403039010	ASAS J002511+1217.2	112.92	−50.08	33.2	>20	5.7	$0.26^{+0.05}_{-0.06}$	$2.5^{+0.7}_{-0.6}$	>−0.60	1	2.0	0.1	<18.0	1	$14.1^{+0.4}_{-0.4}$	2726.8/2518
24	705046010	IRAS 00397−1312	113.89	−75.66	58.5	>20	1.8	$0.24^{+0.06}_{-0.09}$	$1.7^{+3.2}_{-0.5}$	<0.97	1	1.5	0.1	<20.0	1	$10.6^{+0.3}_{-0.3}$	2760.8/2518
25	407039010	EUVE J1439+75.0	114.11	40.14	10.9	>50	3.3	$0.25^{+0.03}_{-0.03}$	$3.4^{+1.1}_{-0.9}$	$0.05^{+0.49}_{-0.28}$	1	3.1	0.1	$22.0^{+5.3}_{-5.5}$	1	$7.8^{+0.3}_{-0.3}$	2865.2/2518
26	706005010	NGC 6251_LOBE_BGD2	115.82	31.61	10.8	>20	6.0	$0.31^{+0.03}_{-0.03}$	$3.9^{+0.6}_{-0.6}$	$0.22^{+0.23}_{-0.16}$	1	3.6	0.1	$19.2^{+3.1}_{-3.0}$	1	$9.3^{+0.5}_{-0.5}$	5618.3/5040
...	706005020	NGC 6251_LOBE_BGD2	115.79	31.61	11.2	>20	6.0	...	...	...	...	...	...	...	...	...	...
27	706004010	NGC 6251_LOBE_BGD1	116.19	31.04	18.8	>20	7.9	$0.29^{+0.03}_{-0.03}$	$4.3^{+0.7}_{-0.7}$	>−0.35	1	3.6	0.1	$32.6^{+3.6}_{-3.5}$	1	$8.4^{+0.4}_{-0.4}$	2924.4/2518
28	705012010	EMS 1160	120.03	27.94	18.2	>30	8.6	$0.32^{+0.08}_{-0.08}$	$2.3^{+0.8}_{-0.7}$	<0.87	1	2.4	0.1	$24.6^{+3.6}_{-3.5}$	1	$12.1^{+0.5}_{-0.5}$	2874.4/2518
29	405034010	EG AND	121.55	−22.18	100.3	>20	13.0	$0.29^{+0.01}_{-0.01}$	$5.2^{+0.4}_{-0.4}$	$0.23^{+0.11}_{-0.09}$	1	4.6	0.1	$28.3^{+1.5}_{-1.5}$	1	$9.3^{+0.2}_{-0.2}$	2603.7/2518
30	706037010	MRK 231	121.76	60.26	83.9	>50	1.0	$0.25^{+0.07}_{-0.07}$	$0.9^{+0.4}_{-0.4}$	<0.51	1	0.9	0.1	$24.7^{+2.4}_{-2.4}$	1	$10.7^{+0.2}_{-0.2}$	2645.9/2518
31	708039010	VII ZW 403	127.83	37.32	67.3	>50	3.9	$0.19^{+0.01}_{-0.01}$	$7.3^{+1.4}_{-1.4}$	<0.11	1	5.2	0.1	<15.8	1	$11.3^{+0.2}_{-0.2}$	2619.2/2518
32	705024010	IRAS 01250+2832	132.51	−33.40	57.6	>20	8.2	$0.26^{+0.04}_{-0.04}$	$3.1^{+0.6}_{-0.6}$	$0.21^{+0.28}_{-0.31}$	1	2.7	0.1	$14.8^{+2.6}_{-2.3}$	1	$9.7^{+0.3}_{-0.3}$	2704.1/2518
33	709003010	NGC 2655	134.94	32.69	25.1	>70	2.4	$0.31^{+0.02}_{-0.02}$	$3.8^{+0.4}_{-0.4}$	$0.32^{+0.11}_{-0.09}$	1	3.3	0.1	$26.2^{+2.7}_{-2.7}$	1	$10.0^{+0.2}_{-0.2}$	2565.1/2518
34	705054010	NGC 3147	136.30	39.48	120.1	>20	3.3	$0.26^{+0.02}_{-0.02}$	$2.6^{+0.4}_{-0.4}$	$0.24^{+0.20}_{-0.15}$	1	2.2	0.1	$21.8^{+2.1}_{-2.1}$	1	$10.9^{+0.2}_{-0.2}$	2554.8/2518
35	505044010	L139_B-32	138.76	−32.31	83.8	>20	6.9	$0.25^{+0.03}_{-0.03}$	$2.4^{+0.4}_{-0.4}$	$0.12^{+0.35}_{-0.23}$	1	2.1	0.1	$16.5^{+1.9}_{-1.9}$	1	$7.8^{+0.2}_{-0.2}$	2638.8/2518
36	506025010	3C 59 VICINITY 2	141.95	−31.19	125.6	>50	6.6	$0.24^{+0.02}_{-0.01}$	$2.9^{+0.4}_{-0.4}$	$0.05^{+0.27}_{-0.19}$	1	2.5	0.1	$16.2^{+1.5}_{-1.5}$	1	$9.4^{+0.2}_{-0.2}$	2690.8/2518
37	506024010	3C 59 VICINITY 1	142.14	−29.91	41.9	>40	7.2	$0.19^{+0.01}_{-0.01}$	$5.9^{+1.5}_{-1.5}$	0.0 (fixed)	1	3.9	0.1	<18.1	1	$7.5^{+0.3}_{-0.3}$	2654.1/2519
38	407043010	CH UMA	142.91	42.66	45.2	>20	4.7	$0.15^{+0.02}_{-0.00}$	$10.9^{+1.4}_{-4.2}$	0.0 (fixed)	1	4.4	0.1	<28.4	1	$9.9^{+0.3}_{-0.3}$	2843.7/2519
39	803041010	NGC 1961 BACKGROUND	145.25	18.81	24.1	>20	13.1	$0.25^{+0.04}_{-0.02}$	$3.7^{+0.8}_{-0.9}$	>−0.61	1	3.1	0.1	<7.4	1	$8.2^{+0.4}_{-0.4}$	2830.7/2518
40	705003010	1150+497	145.52	64.98	105.6	>20	2.2	$0.15^{+0.02}_{-0.00}$	$5.8^{+0.7}_{-2.4}$	<0.05	1	3.0	0.1	<25.0	1	$11.6^{+0.2}_{-0.2}$	2583.6/2518
41	704048010	NGC 3718	146.88	60.21	49.9	>30	1.1	$0.22^{+0.01}_{-0.03}$	$1.9^{+1.3}_{-0.4}$	0.0 (fixed)	1	1.5	0.1	<16.1	1	$11.0^{+0.3}_{-0.3}$	2615.6/2519
42	100046010	LOCKMAN HOLE	148.98	53.15	66.4	>30	0.6	$0.26^{+0.01}_{-0.02}$	$1.4^{+0.2}_{-0.1}$	$0.08^{+0.21}_{-0.15}$	1	1.3	0.1	$16.2^{+0.9}_{-1.0}$	1	$11.3^{+0.2}_{-0.2}$	13261.7/ 12606
...	101002010	LOCKMAN HOLE	149.70	53.20	39.7	>40	0.6	...	...	...	...	...	...	...	...	...	...

Table 1
(Continued)

Region (1)	Sequence (2)	Target Name (3)	l (4)	b (5)	t (6)	DYE (7)	N_H (8)	kT_{halo} (9)	EM_{halo} (10)	$[O/Fe]_{halo}$ (11)	Z_{halo} (12)	S_{halo} (13)	kT_{local} (14)	EM_{local} (15)	Z_{local} (16)	N_{CXB} (17)	C/dof (18)
...	102018010	LOCKMAN HOLE	149.71	53.19	90.3	>30	0.6	...	...	...	...	...	...	...	...	...	...
...	103009010	LOCKMAN HOLE	149.70	53.20	71.7	>20	0.6	...	...	...	...	...	...	...	...	...	...
...	104002010	LOCKMAN HOLE	149.70	53.20	92.1	>20	0.6	...	...	...	...	...	...	...	...	...	...
43	504062010	VICINITY OF NGC 4051	150.13	70.30	89.5	>20	1.2	$0.29^{+0.03}_{-0.03}$	$1.9^{+0.3}_{-0.4}$	$0.33^{+0.22}_{-0.15}$	1	1.6	0.1	$16.3^{+1.7}_{-1.7}$	1	$10.8^{+0.2}_{-0.2}$	2509.1/2518
44	704013010	2MASX J02485937+2630	153.13	−29.32	43.2	>20	15.2	$0.30^{+0.04}_{-0.04}$	$2.4^{+0.6}_{-0.6}$	$0.02^{+0.50}_{-0.30}$	1	2.5	0.1	$16.1^{+1.9}_{-1.9}$	1	$10.5^{+0.4}_{-0.4}$	2714.9/2518
45	705001010	MRK 18	155.86	39.40	38.0	>20	5.0	$0.25^{+0.07}_{-0.7}$	$1.7^{+1.6}_{-0.7}$	0.0 (fixed)	1	1.6	0.1	<28.3	1	$12.5^{+0.4}_{-0.4}$	2761.7/2519
46	707021010	AO 0235+164	156.78	−39.11	26.2	>50	10.3	$0.18^{+0.02}_{-0.02}$	$5.9^{+3.6}_{-2.2}$	0.0 (fixed)	1	3.6	0.1	<21.6	1	$8.8^{+0.3}_{-0.3}$	2725.8/2519
47	501104010	MBM 12 OFF-CLOUD	157.34	−36.82	20.1	>20	9.0	$0.20^{+0.03}_{-0.02}$	$3.1^{+1.5}_{-1.2}$	0.0 (fixed)	1	2.2	0.1	<17.6	1	$7.5^{+0.4}_{-0.4}$	2745.4/2519
48	402046010	BZ UMA	159.02	38.83	29.7	>20	4.8	$0.34^{+0.06}_{-0.06}$	$2.1^{+0.6}_{-0.6}$	>−0.57	1	1.6	0.1	$11.6^{+2.5}_{-2.7}$	1	$11.8^{+0.6}_{-0.6}$	2756.5/2518
49	709021010	I ZW 18	160.54	44.84	16.6	>30	2.7	$0.14^{+0.01}_{-0.00}$	$16.4^{+1.9}_{-4.5}$	0.0 (fixed)	1	5.5	0.1	<29.6	1	$8.2^{+0.3}_{-0.4}$	2831.9/2519
50	703065010	IRAS F01475−0740	160.70	−65.86	57.9	>20	2.2	$0.22^{+0.06}_{-0.03}$	<4.7	0.0 (fixed)	1	0.5	0.1	<14.3	1	$9.3^{+0.3}_{-0.3}$	2738.0/2519
51	704052010	SDSS J0943+5417	161.23	46.42	34.2	>20	1.5	$0.34^{+0.05}_{-0.04}$	$2.0^{+0.4}_{-0.4}$	>−0.14	1	1.7	0.1	$16.1^{+2.2}_{-2.5}$	1	$10.0^{+0.4}_{-0.3}$	2700.7/2518
52	709019010	Q0142-100	161.64	−68.48	56.7	>30	3.2	$0.19^{+0.10}_{-0.03}$	$2.8^{+3.4}_{-1.6}$	<0.62	1	2.1	0.1	$11.4^{+4.8}_{-6.4}$	1	$9.7^{+0.2}_{-0.2}$	2623.4/2518
53	402044010	SW UMA	164.81	36.96	16.9	>20	4.1	$0.65^{+0.09}_{-0.23}$	$3.4^{+0.8}_{-0.8}$	>−0.10	1	2.9	0.1	$14.0^{+2.5}_{-2.4}$	1	$7.8^{+0.6}_{-0.6}$	2799.3/2518
54	509008010	HOT BLOB 2	164.90	38.21	21.4	>80	3.2	$0.23^{+0.02}_{-0.02}$	$3.4^{+0.9}_{-0.7}$	$−0.21^{+0.69}_{-0.44}$	1	3.1	0.1	$16.1^{+3.3}_{-3.5}$	1	$9.5^{+0.2}_{-0.2}$	2598.3/2518
55	701057010	APM 08279+5255	165.74	36.24	85.2	>20	4.7	$0.31^{+0.02}_{-0.02}$	$1.7^{+0.1}_{-0.1}$	$0.35^{+0.08}_{-0.08}$	1	1.5	0.1	$12.9^{+0.7}_{-0.7}$	1	$10.4^{+0.2}_{-0.2}$	7972.2/7562
...	701057020	APM 08279+5255	165.74	36.24	64.1	>30	4.7	...	...	...	...	...	...	...	...	...	...
...	701057030	APM 08279+5255	165.76	36.24	104.3	>20	4.7	...	...	...	...	...	...	...	...	...	...
56	508073010	MBM 16-OFF	165.86	−38.39	78.2	>30	19.0	$0.19^{+0.04}_{-0.03}$	$5.4^{+2.2}_{-2.0}$	<0.91	1	3.7	0.1	$9.7^{+2.2}_{-2.1}$	1	$8.8^{+0.2}_{-0.2}$	2568.6/2518
57	505058010	L168_B53	167.64	53.19	46.3	>40	0.9	$0.18^{+0.01}_{-0.01}$	$4.4^{+1.3}_{-1.3}$	0.0 (fixed)	1	2.7	0.1	<26.9	1	$8.3^{+0.2}_{-0.2}$	2463.3/2519
58	509009010	HOT BLOB 3	167.88	36.01	18.4	>80	5.0	$0.24^{+0.04}_{-0.03}$	$1.8^{+0.8}_{-0.7}$	<0.36	1	1.7	0.1	$19.5^{+3.3}_{-3.3}$	1	$8.0^{+0.2}_{-0.2}$	2585.9/2518
59	703042010	J081618.99+482328.4	171.02	33.70	90.9	>20	5.8	$0.28^{+0.03}_{-0.02}$	$1.6^{+0.3}_{-0.3}$	$0.09^{+0.31}_{-0.23}$	1	1.6	0.1	$8.9^{+1.3}_{-0.6}$	1	$10.5^{+0.2}_{-0.2}$	2612.3/2518
60	709009010	ARP 318	173.96	−64.97	77.3	>30	2.8	$0.32^{+0.02}_{-0.02}$	$3.4^{+0.3}_{-0.3}$	$0.17^{+0.13}_{-0.10}$	1	3.3	0.1	$15.0^{+1.5}_{-1.5}$	1	$10.9^{+0.2}_{-0.2}$	2717.3/2518
61	703008010	SWIFT J0911.2+4533	174.71	43.11	76.6	>20	1.3	$0.22^{+0.02}_{-0.02}$	$1.8^{+0.5}_{-0.5}$	<0.79	1	1.5	0.1	<15.0	1	$9.7^{+0.2}_{-0.2}$	2628.6/2518
62	706013010	3C 78	174.85	−44.51	96.1	>20	14.6	$0.39^{+0.02}_{-0.02}$	$6.4^{+0.4}_{-0.4}$	$0.62^{+0.04}_{-0.04}$	1	5.3	0.1	$11.0^{+1.2}_{-1.2}$	1	$9.9^{+0.2}_{-0.2}$	2714.8/2518
63	706038010	IRAS 09104+4109	180.99	43.55	72.7	>40	1.5	$0.30^{+0.03}_{-0.04}$	$1.8^{+0.3}_{-0.3}$	>−0.74	1	1.4	0.1	$17.5^{+1.8}_{-1.8}$	1	$10.9^{+0.2}_{-0.2}$	2614.7/2518
64	709007010	SWIFT J0714.2+3518	182.49	19.57	47.9	>90	6.7	$0.22^{+0.02}_{-0.02}$	$2.5^{+0.6}_{-0.5}$	<0.30	1	2.3	0.1	$13.8^{+1.9}_{-1.8}$	1	$8.4^{+0.2}_{-0.2}$	2819.4/2518
65	704053010	IC 2497	190.27	48.82	76.3	>20	1.1	$0.33^{+0.04}_{-0.04}$	$1.8^{+0.3}_{-0.3}$	>−0.08	1	1.5	0.1	$17.6^{+1.8}_{-1.8}$	1	$10.5^{+0.3}_{-0.3}$	2631.1/2518
66	707006010	3C 236 BACKGROUND	190.35	53.69	25.7	>30	1.0	$0.18^{+0.02}_{-0.01}$	$4.9^{+1.6}_{-1.6}$	0.0 (fixed)	1	3.1	0.1	<30.8	1	$8.4^{+0.3}_{-0.3}$	2863.1/2519
67	708038010	IRAS F11119+3257	192.21	68.35	142.9	>70	2.2	$0.19^{+0.01}_{-0.01}$	$4.1^{+0.8}_{-0.8}$	$−0.11^{+0.63}_{-0.36}$	1	2.9	0.1	$10.2^{+2.6}_{-2.6}$	1	$9.2^{+0.1}_{-0.1}$	2608.1/2518
68	409029010	1RXS J032540.0−08144	192.87	−48.95	36.4	>30	5.9	$0.23^{+0.01}_{-0.01}$	$15.6^{+0.9}_{-0.9}$	$0.51^{+0.09}_{-0.08}$	1	11.7	0.1	$22.0^{+3.5}_{-3.4}$	1	$10.7^{+0.3}_{-0.3}$	2818.1/2518
69	700011010	SWIFT J0746.3+2548	194.52	22.92	100.1	>20	5.1	$0.26^{+0.02}_{-0.02}$	$2.2^{+0.3}_{-0.3}$	$−0.01^{+0.31}_{-0.21}$	1	2.1	0.1	$13.4^{+1.1}_{-1.1}$	1	$10.8^{+0.2}_{-0.2}$	2728.2/2518
70	703003010	Q0827+243	200.02	31.88	48.2	>20	3.3	$0.46^{+0.13}_{-0.09}$	$1.4^{+0.4}_{-0.4}$	<0.90	1	1.5	0.1	$10.3^{+1.8}_{-1.9}$	1	$11.7^{+0.4}_{-0.4}$	2572.3/2518
71	407045010	BF ERI	201.04	−31.30	28.3	>20	5.8	$0.30^{+0.02}_{-0.02}$	$7.3^{+0.7}_{-0.7}$	>0.31	1	5.5	0.1	$31.6^{+3.2}_{-3.1}$	1	$11.5^{+0.4}_{-0.4}$	2876.9/2518
72	404035010	HD 72779	205.51	31.34	71.0	>20	2.9	$0.64^{+0.05}_{-0.05}$	$2.3^{+0.4}_{-0.4}$	$0.45^{+0.10}_{-0.08}$	1	2.3	0.1	$17.4^{+1.5}_{-1.5}$	1	$8.2^{+0.3}_{-0.3}$	2632.5/2518
73	408029010	V1159 ORI	206.53	−19.94	76.0	>90	27.6	$0.31^{+0.01}_{-0.01}$	$10.5^{+0.6}_{-0.6}$	$0.33^{+0.05}_{-0.04}$	1	9.2	0.1	$21.3^{+1.2}_{-1.2}$	1	$12.0^{+0.2}_{-0.2}$	2623.6/2518
74	708044010	B2 1023+25	207.06	57.61	59.5	>30	1.7	$0.18^{+0.01}_{-0.01}$	$5.9^{+1.1}_{-1.2}$	<0.25	1	3.9	0.1	<24.4	1	$8.6^{+0.2}_{-0.2}$	2749.9/2518
75	702062010	Q0450-1310	211.75	−32.07	15.5	>20	10.3	$0.40^{+0.13}_{-0.07}$	$3.6^{+0.7}_{-0.7}$	>−0.13	1	3.4	0.1	$15.0^{+2.8}_{-2.7}$	1	$11.4^{+0.6}_{-0.6}$	2831.6/2518
76	809052010	OFF-FIELD1	212.25	55.01	37.9	>40	2.1	$0.33^{+0.06}_{-0.05}$	$2.9^{+0.4}_{-0.4}$	$0.26^{+0.19}_{-0.13}$	1	2.7	0.1	$24.4^{+2.8}_{-2.3}$	1	$10.5^{+0.3}_{-0.3}$	2694.7/2518
77	702115010	IRAS 10565+2448	212.34	64.73	39.4	>20	1.1	$0.35^{+0.04}_{-0.04}$	$1.8^{+0.3}_{-0.3}$	$0.33^{+0.21}_{-0.13}$	1	1.7	0.1	$18.1^{+1.7}_{-1.7}$	1	$8.1^{+0.3}_{-0.3}$	2721.9/2518
78	502076010	ERIDANUS HOLE	213.44	−39.09	103.7	>20	2.6	$0.26^{+0.03}_{-0.03}$	$1.6^{+0.3}_{-0.3}$	$0.05^{+0.36}_{-0.13}$	1	1.5	0.1	$14.4^{+1.4}_{-1.5}$	1	$7.9^{+0.2}_{-0.2}$	2591.2/2518
79	707007010	2FGL J0923.5+1508	215.97	40.48	91.5	>30	3.2	$0.15^{+0.03}_{-0.02}$	$6.8^{+3.1}_{-3.2}$	<0.35	1	3.2	0.1	<19.5	1	$10.6^{+0.2}_{-0.2}$	2519.9/2518
80	409030010	IW ERIDANI	216.44	−40.61	28.9	>40	2.8	$0.15^{+0.01}_{-0.01}$	$8.9^{+1.1}_{-1.1}$	0.0 (fixed)	1	3.7	0.1	<10.7	1	$8.7^{+0.3}_{-0.3}$	2939.0/2519
81	708002010	NGC 3997	218.72	77.83	80.8	>40	1.7	$0.19^{+0.02}_{-0.01}$	$5.6^{+1.1}_{-2.1}$	$0.06^{+0.47}_{-0.30}$	1	3.8	0.1	<21.9	1	$10.6^{+0.2}_{-0.2}$	2739.3/2518
82	704039010	PKS 0326−288	224.90	−55.40	56.5	>20	1.0	$0.20^{+0.03}_{-0.03}$	$2.0^{+1.2}_{-0.7}$	0.0 (fixed)	1	1.4	0.1	<22.2	1	$8.5^{+0.2}_{-0.2}$	2676.8/2519
83	702076010	SWIFT J0918.5+0425	227.10	34.42	52.8	>20	3.8	$0.29^{+0.03}_{-0.03}$	$1.8^{+0.3}_{-0.3}$	>−0.47	1	1.5	0.1	$12.3^{+1.6}_{-1.7}$	1	$9.8^{+0.3}_{-0.3}$	2689.3/2518
84	702064010	Q1017+1055	230.36	50.83	18.0	>20	3.4	$0.21^{+0.04}_{-0.06}$	<327.0	0.0 (fixed)	1	0.7	0.1	<16.0	1	$10.6^{+0.5}_{-0.5}$	2880.2/2519
85	901005010	GRB070328	235.19	−44.99	52.6	>20	2.9	$0.40^{+0.05}_{-0.05}$	$1.6^{+0.3}_{-0.3}$	$0.35^{+0.19}_{-0.12}$	1	1.6	0.1	$9.7^{+1.3}_{-1.3}$	1	$9.1^{+0.3}_{-0.3}$	2815.5/2518
86	709020020	HE 0512−3329	236.64	−33.86	16.1	>50	2.6	$0.31^{+0.04}_{-0.03}$	$2.6^{+0.4}_{-0.4}$	$0.26^{+0.20}_{-0.14}$	1	2.4	0.1	$26.3^{+2.4}_{-2.4}$	1	$9.2^{+0.4}_{-0.4}$	5729.4/5040

5

Table 1
(Continued)

Region (1)	Sequence (2)	Target Name (3)	l (4)	b (5)	t (6)	DYE (7)	N_H (8)	kT_{halo} (9)	EM_{halo} (10)	$[O/Fe]_{halo}$ (11)	Z_{halo} (12)	S_{halo} (13)	kT_{local} (14)	EM_{local} (15)	Z_{local} (16)	N_{CXB} (17)	C/dof (18)
...	709020030	HE 0512−3329	236.62	−33.85	13.6	>60	2.6	...	...	...	...	...	...	...	...	...	...
87	506056010	G236+38 OFF	237.07	41.12	62.5	>20	2.1	$0.18^{+0.01}_{-0.03}$	$5.7^{+4.8}_{-1.4}$	>-0.85	1	3.5	0.1	<23.2	1	$7.9^{+0.2}_{-0.2}$	2695.3/2518
88	702031010	MRK 1239	239.27	38.22	26.1	>20	4.4	$0.32^{+0.15}_{-0.07}$	$1.0^{+0.4}_{-0.4}$	<0.76	1	1.2	0.1	$23.0^{+2.5}_{-2.3}$	1	$9.2^{+0.4}_{-0.2}$	2785.3/2518
89	503104010	ARC_BACKGROUND	240.49	−66.02	167.0	>20	4.1	$0.27^{+0.01}_{-0.04}$	$1.0^{+0.3}_{-0.2}$	$0.02^{+0.56}_{-1.3}$	1	1.0	0.1	$12.1^{+1.0}_{-1.3}$	1	$8.5^{+0.2}_{-0.2}$	2508.9/2518
90	405014010	PSR J0614−33	240.50	−21.83	31.1	>20	3.9	$0.35^{+0.03}_{-0.02}$	$4.4^{+0.5}_{-0.5}$	$0.37^{+0.11}_{-0.09}$	1	3.9	0.1	$18.4^{+2.5}_{-2.4}$	1	$8.3^{+0.4}_{-0.4}$	2813.0/2518
91	703036020	Q0551−3637	242.37	−26.92	21.6	>20	3.6	$0.31^{+0.04}_{-0.04}$	$2.8^{+0.5}_{-0.5}$	>-0.11	1	2.1	0.1	$16.0^{+2.8}_{-2.8}$	1	$10.2^{+0.4}_{-0.4}$	2839.2/2518
92	703040010	Q0940−1050	246.39	30.44	32.4	>20	4.6	$0.40^{+0.04}_{-0.04}$	$2.7^{+0.3}_{-0.4}$	>0.23	1	1.9	0.1	$18.4^{+2.1}_{-2.1}$	1	$11.1^{+0.4}_{-0.4}$	2656.8/2518
93	703062010	NGC 1448	251.60	−51.38	53.0	>20	1.0	$0.20^{+0.06}_{-0.04}$	$1.9^{+3.0}_{-0.7}$	<0.62	1	1.6	0.1	<24.8	1	$10.9^{+0.3}_{-0.3}$	2513.7/2518
94	703016010	SWIFT J0134.1−3625	261.71	−77.06	33.0	>40	2.1	$0.46^{+0.04}_{-0.05}$	$2.7^{+0.4}_{-0.4}$	$0.54^{+0.08}_{-0.07}$	1	2.4	0.1	$15.9^{+2.0}_{-2.0}$	1	$10.5^{+0.3}_{-0.3}$	2650.4/2518
95	707012010	NGC 3431	266.04	37.10	55.1	>60	4.8	$0.15^{+0.01}_{-0.01}$	$11.9^{+4.3}_{-4.4}$	0.0 (fixed)	1	4.7	0.1	<27.4	1	$13.1^{+0.3}_{-0.3}$	2690.2/2519
96	808057010	BULLET-BKG	266.15	−20.78	43.1	>40	6.8	$0.25^{+0.02}_{-0.02}$	$4.3^{+0.6}_{-0.6}$	$0.28^{+0.21}_{-0.15}$	1	3.5	0.1	$21.1^{+2.5}_{-2.5}$	1	$8.6^{+0.3}_{-0.3}$	2753.6/2518
97	708004010	ESO 119-G008	266.67	−38.88	44.6	>50	1.3	$0.23^{+0.01}_{-0.02}$	$3.9^{+1.2}_{-0.5}$	$0.08^{+0.39}_{-0.20}$	1	3.2	0.1	$24.5^{+2.9}_{-2.9}$	1	$8.2^{+0.2}_{-0.2}$	2634.3/2518
98	708043010	NGC 3660	269.10	48.36	81.4	>50	4.0	$0.31^{+0.02}_{-0.02}$	$4.0^{+0.3}_{-0.3}$	$0.44^{+0.08}_{-0.07}$	1	3.3	0.1	$24.1^{+1.7}_{-1.7}$	1	$10.4^{+0.2}_{-0.2}$	2581.7/2518
99	500027020	HIGH LAT. DIFFUSE B	272.40	−58.27	50.7	>30	3.3	$0.33^{+0.03}_{-0.03}$	$1.4^{+0.2}_{-0.2}$	>0.07	1	1.1	0.1	$12.3^{+1.1}_{-1.1}$	1	$7.8^{+0.3}_{-0.3}$	2676.6/2518
100	701008010	IRAS F11223−1244	272.55	44.74	40.9	>20	4.8	$0.25^{+0.04}_{-0.03}$	$2.0^{+0.5}_{-0.5}$	$0.03^{+0.73}_{-2.2}$	1	1.8	0.1	$20.3^{+2.3}_{-2.2}$	1	$9.1^{+0.3}_{-0.3}$	2817.0/2518
101	703037010	Q0109−3518	275.46	−80.96	30.0	>20	2.0	$0.25^{+0.06}_{-0.02}$	$1.4^{+0.9}_{-0.5}$	$-0.15^{+2.68}_{-0.71}$	1	1.4	0.1	$19.5^{+3.0}_{-3.8}$	1	$9.0^{+0.4}_{-0.4}$	2772.5/2518
102	703002010	PKS 0208−512	276.10	−61.79	51.9	>20	1.9	$0.22^{+0.01}_{-0.02}$	$2.7^{+1.1}_{-0.4}$	>-0.82	1	2.1	0.1	<19.4	1	$9.6^{+0.3}_{-0.3}$	2717.3/2518
103	504069010	SEP #1	276.40	−29.82	37.4	>20	5.8	$0.26^{+0.02}_{-0.01}$	$5.3^{+0.4}_{-0.4}$	$0.31^{+0.07}_{-0.06}$	1	4.4	0.1	$22.2^{+1.7}_{-1.7}$	1	$8.6^{+0.2}_{-0.2}$	11009.3/ 10084
...	504071010	SEP #2	276.40	−29.82	52.5	>20	5.8	...	...	...	...	...	...	...	...	...	...
...	504073010	SEP #3	276.39	−29.83	40.8	>30	5.8	...	...	...	...	...	...	...	...	...	...
...	504075010	SEP #4	276.39	−29.82	49.7	>20	5.8	...	...	...	...	...	...	...	...	...	...
104	501002010	SKY_53.3_-63.4	278.62	−45.31	92.3	>20	5.8	$0.29^{+0.01}_{-0.01}$	$4.5^{+0.2}_{-0.2}$	$0.38^{+0.07}_{-0.06}$	1	3.7	0.1	$16.1^{+1.0}_{-1.0}$	1	$9.1^{+0.2}_{-0.2}$	2675.4/2518
105	501001010	SKY_50.0_-62.4	278.68	−47.08	80.1	>20	2.4	$0.25^{+0.01}_{-0.01}$	$5.2^{+0.3}_{-0.2}$	$0.30^{+0.09}_{-0.07}$	1	4.2	0.1	$27.9^{+1.7}_{-1.7}$	1	$7.5^{+0.2}_{-0.2}$	2767.8/2518
106	402089020	TW HYA	278.68	22.95	20.0	>20	6.8	$0.28^{+0.02}_{-0.02}$	$9.7^{+0.9}_{-0.8}$	$0.28^{+0.13}_{-0.11}$	1	8.3	0.1	$26.2^{+3.6}_{-3.5}$	1	$10.9^{+0.5}_{-0.5}$	2875.2/2518
107	705045010	IRAS 12072−0444	283.97	56.32	57.5	>20	3.5	$0.15^{+0.02}_{-0.01}$	$8.4^{+3.6}_{-3.7}$	<0.15	1	4.2	0.1	<28.1	1	$9.0^{+0.2}_{-0.2}$	2642.8/2518

Note. Column (1): region numbers. Column (2): sequence numbers of the *Suzaku* archive. Column (3): target names shown in the event headers. Column (4): Galactic longitude for the aim points in units of degrees. Column (5): Galactic latitude for the aim points in units of degrees. Column (6): effective exposure times after the screening in units of ks. Column (7): screening criteria for the DYE_ELV cut in units of degrees. Column (8): fixed hydrogen column densities calculated according to Willingale et al. (2013) in units of 10^{20} cm^{-2}. Column (9): temperatures for the hot gaseous halo in units of keV. Column (10): emission measures for the hot gaseous halo in units of 10^{-2} cm^{-6} pc. Column (11): abundance ratios of oxygen to iron for the hot gaseous halo in units of dex. Column (12): metal abundance relative to the solar value except for Fe. Column (13): unabsorbed surface brightness of the Galactic gaseous halo component in the 0.4–1.0 keV band. Units are 10^{-12} erg cm^{-2} s^{-1} deg^2. Column (14): fixed temperatures for the local component in units of keV. Column (15): emission measures for the local component in units of 10^{-2} cm^{-6} pc. Column (16): fixed metal abundance relative to the solar value. Column (17): normalizations at 1 keV for the CXB component in units of photons cm^{-2} s^{-1} sr^{-1}. Column (18): best-fit C-statistics and degree of freedom.

(This table is available in machine-readable form.)

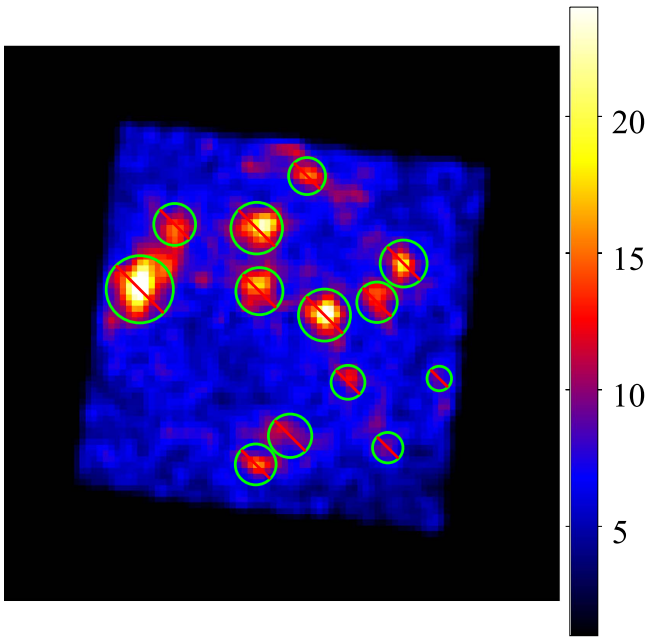**Figure 2.** XIS count image in the 0.7–5.0 keV band for ObsID 502047010 (region #7) aiming at $(l, b) = (86°.0, -20°.8)$. The data of XIS 0, XIS 1, and XIS 3 were co-added. The vignetting effect was not corrected, and Gaussian smoothing with $\sigma = 16''$ was applied. Point-source candidates detected by the `wavdetect` tool are shown in the green circles.
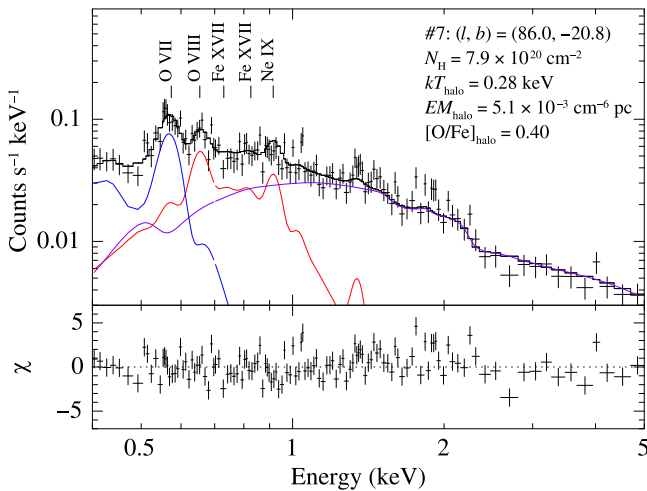

Figure 3. Top panel shows the XIS1 spectrum of ObsID 502047010 (region #7). For plotting purposes, the spectrum is binned so that each bin has at least 25 counts after subtracting the instrumental background. The black curve is the best-fit model, which consists of three components: the Galactic hot gaseous halo (red), the local emission component (blue), and the CXB (purple). The bottom panel shows the residuals between the data and the model.

maximum is 16.4×10^{-3} cm^{-6} pc, and the median is 3.1×10^{-3} cm^{-6} pc. As shown in Table 2, no significant correlation was found between EM$_{halo}$ and $|l|$, whereas a weak negative correlation of $\rho = -0.25$ was found between EM$_{halo}$ and $|b|$, with a p-value of 0.012.

Figure 7 is the same as Figure 4, but for [O/Fe]$_{halo}$. Because [O/Fe]$_{halo}$ is constrained in only 46 out of 107 regions, the histogram is drawn for those 46 fields. The median is 0.25, and the 16th–84th percentile range is 0.03–0.37. We found no significant correlation between [O/Fe]$_{halo}$ and the Galactic coordinates (Table 2).

The 68% interval with the median of N_{CXB} is $9.0^{+1.0}_{-1.4}$ photons cm^{-2} s^{-1} sr^{-1} keV^{-1}. The median value is ~10% lower than the value reported by Cappelluti et al. (2017) but is within the systematic uncertainty of the different measurements (Moretti et al. 2009). The fluctuation of N_{CXB} is consistent with the cosmic variance expected in the *Suzaku* FOV (~15%).

The range of EM$_{local}$ is $(6.4–33) \times 10^{-3}$ cm^{-6} pc, with a median of 18×10^{-3} cm^{-6} pc. The surface brightness of the local emission component spans $(1.3–6.8) \times 10^{-12}$ erg cm^{-2} s^{-1} deg^{-2} in the 0.4–1.0 keV band. These parameter ranges roughly agree with those obtained by previous observations with *Suzaku* and *XMM-Newton* (Galeazzi et al. 2007; Smith et al. 2007; Henley & Shelton 2015; Ursino et al. 2016).

3.3. Correlations between the Parameters

Correlations between the parameters (EM$_{halo}$, [O/Fe]$_{halo}$, and EM$_{local}$ vs. kT_{halo}) are shown in Figure 8. The corresponding Spearman correlation factors (ρ_{data}) are also shown. The EM$_{halo}$–kT_{halo} and [O/Fe]$_{halo}$–kT_{halo} plots show negative and positive correlations, respectively, whereas the EM$_{local}$–kT_{halo} plot shows no correlation.

These correlations might be artifacts due to intrinsic correlations in the spectral model, because, even if all the fields have the same true values, the obtained fitting parameters may have some correlations due to statistical uncertainties. To investigate this effect, we created 10^4 simulated spectra of XIS1 with a typical exposure time of 50 ks and the median values of the parameters obtained in the previous section. We derived the best-fit parameters from these mock spectra and created statistical contours in Figure 8, which indicated the intrinsic correlations between the parameters. The Spearman correlation factors for the simulated data set (ρ_{sim}) are also shown in Figure 8.

In the plots of EM$_{halo}$–kT_{halo} and EM$_{local}$–kT_{halo}, the scatter of the data points is larger than the contours derived from the simulation, suggesting that the observed scatters do not originate from intrinsic correlations. On the other hand, the scatter of the data in the [O/Fe]$_{halo}$–kT_{halo} plot agrees with the contours, suggesting that the observed correlation is likely artificial.

4. Discussion

We obtained the temperatures, the emission measures, and the [O/Fe] abundances of the hot gas for the 107 lines of sight. We compared our result with those of previous studies in Section 4.1. The contamination from unresolved stellar sources was estimated in Section 4.2. We then examined the spatial distribution model with our emission measure data in Section 4.3 and discussed the origin of the hot gaseous halo in Section 4.4. We also discussed the metallicity and the high-temperature regions in Sections 4.5 and 4.6, respectively.

4.1. Comparison with Previous Studies

4.1.1. Previous Suzaku Results

Yoshino et al. (2009, hereafter Y09) analyzed 13 *Suzaku* observations, 9 of which are also included in our data set. Before making a comparison with our result, we need to note the differences between their spectral model ("model2") and our model. Y09 used the solar abundance of
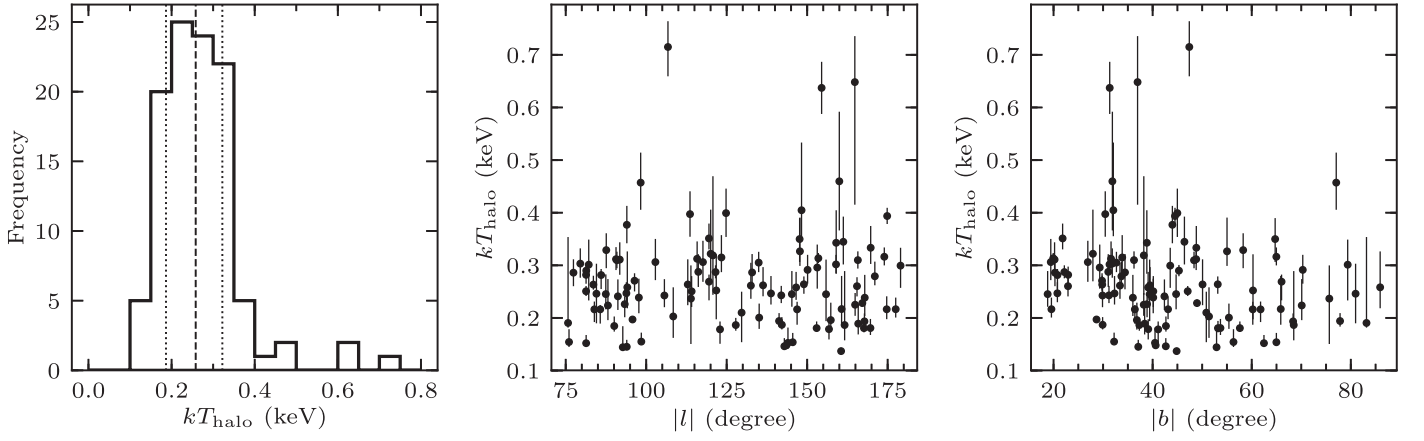
Figure 4. Left: histogram of kT_{halo} derived from the spectral fitting. The vertical dashed line indicates the median, and the vertical dotted lines indicate the 16th and 84th percentiles. Middle and right: kT_{halo} vs. $|l|$ and $|b|$, respectively.
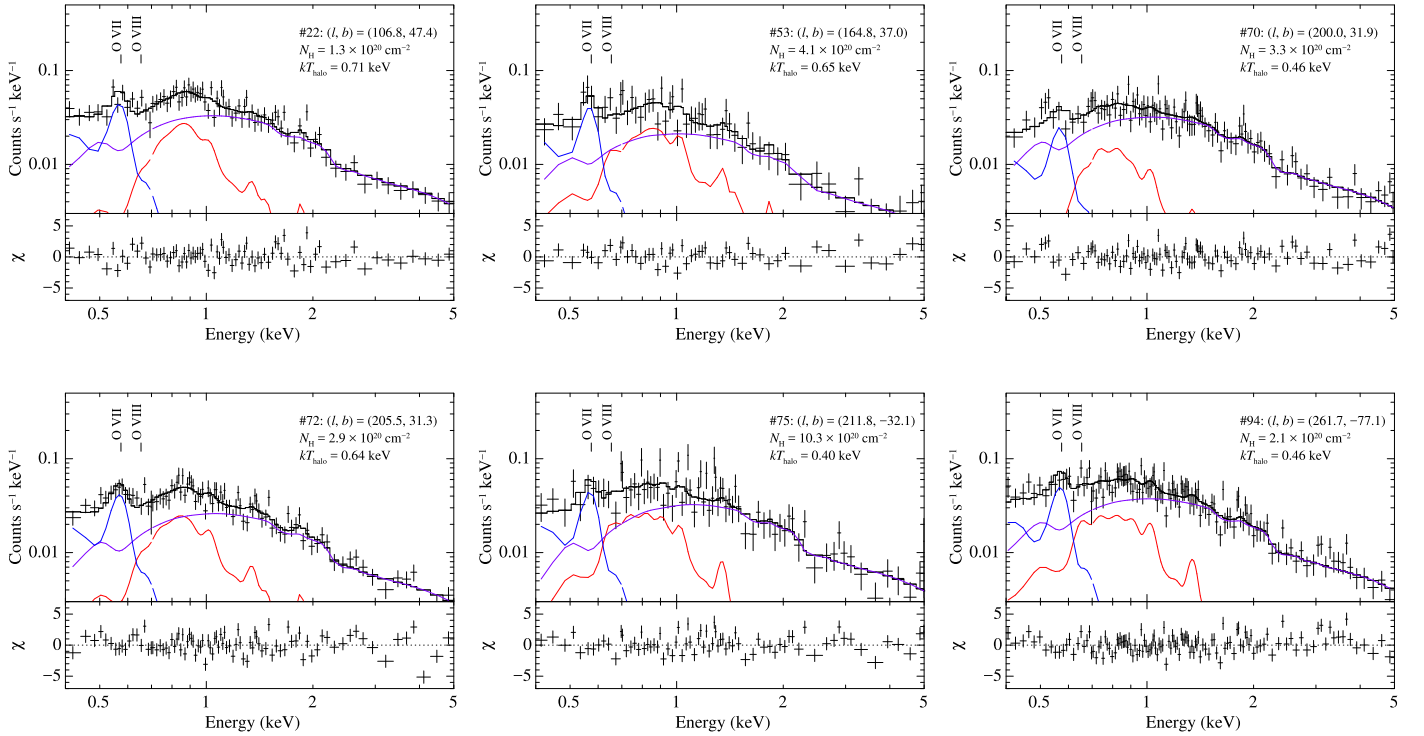

Figure 5. Same as Figure 3, but for regions 22, 53, 70, 72, 75, and 94, which show $kT_{\mathrm{halo}} > 0.4$ keV.

Table 2
Spearman Rank Correlation between the Halo Parameters
and the Galactic Coordinates

	$|l|$		$|b|$	
	ρ	p-value	ρ	p-value
kT_{halo}	0.02	0.79	-0.24	0.019
$\mathrm{EM}_{\mathrm{halo}}$	-0.09	0.39	-0.24	0.012
$[\mathrm{O/Fe}]_{\mathrm{halo}}$	0.08	0.53	0.03	0.70

Anders & Grevesse (1989) and the old AtomDB version 1.3.1. They fixed $\mathrm{EM}_{\mathrm{local}}$ to 7×10^{-3} cm^{-6} pc, which is lower than our best-fit median value by a factor of 2.5. The neon abundance is a free parameter in Y09, in contrast to the fixed solar value used in our analysis. Their CXB is modeled by two broken power-law functions instead of a single power-law function. They calculated the absorption column

densities from Dickey & Lockman (1990), which are slightly lower than those from Willingale et al. (2013).

Figure 9 compares our results with those of Y09 using the nine overlapped regions. Y09 analyzed the two Lockman Hole observations (LH-1 and LH-2) and the two north ecliptic pole observations (NEP1 and NEP2) separately; however, we showed only a comparison with the LH-1 and NEP1 results in Figure 9 because the same line-of-sight data were simultaneously fitted in our analysis. We found that for our results kT_{halo} is ~20% higher, $\mathrm{EM}_{\mathrm{halo}}$ is ~60% higher, and Z_{Fe} is 80% lower compared to the Y09 results on average.

These discrepancies result from the model differences described below. First is the lower $\mathrm{EM}_{\mathrm{local}}$ in Y09 compared to our best-fit values. The lower $\mathrm{EM}_{\mathrm{local}}$ deceases kT_{halo} to compensate for the O VII line flux. This tendency is illustrated in the right panel of Figure 8. Second is the difference in the solar abundance. Y09 used the solar abundance of
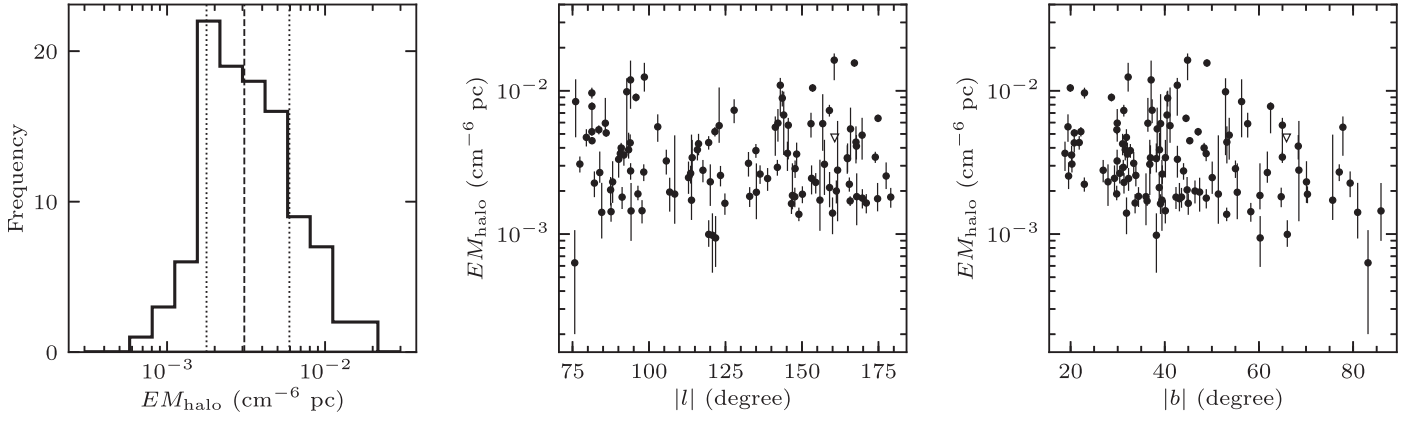
Figure 6. Same as Figure 4, but for EM_{halo}. The 3σ upper limit is shown by the downward-pointing triangles in the middle and right panels. The upper limit is excluded in the left histogram.
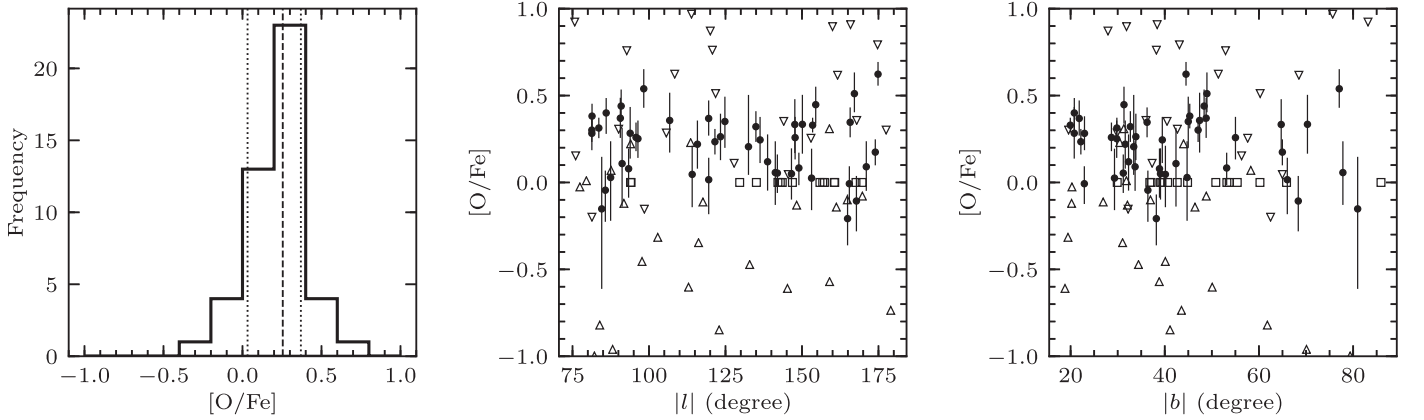
Figure 7. Same as Figure 4, but for $[O/Fe]_{halo}$. In the middle and right panels, the 3σ upper and lower limits are shown by the downward-pointing and upward-pointing triangles, respectively. The fixed values are shown by the squares. The upper and lower limits and fixed values are excluded from the left histogram.
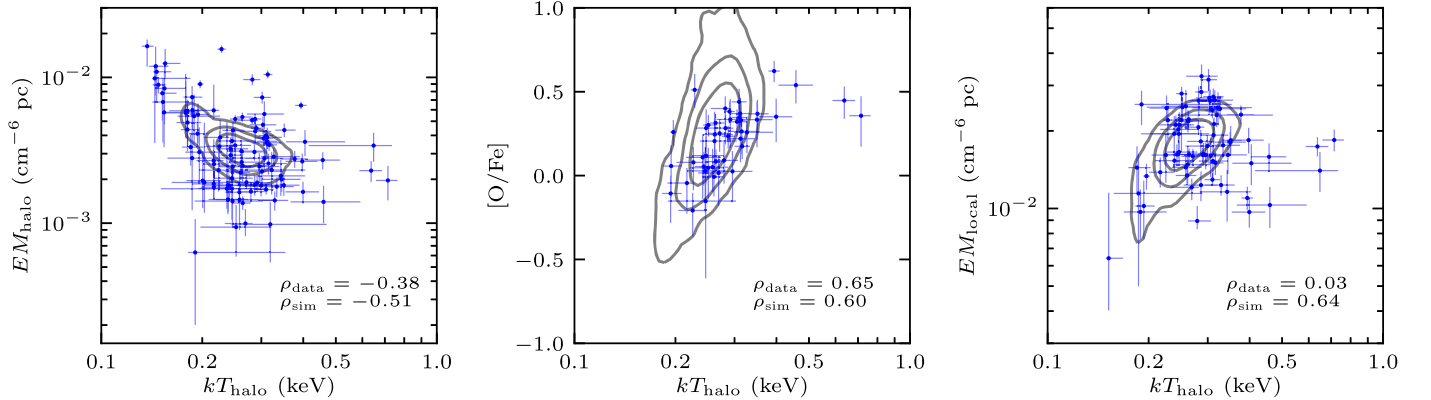
Figure 8. Scatter plots of EM_{halo}, $[O/Fe]_{halo}$, and EM_{local} vs. kT_{halo}. The data of the upper and lower limits are not shown. The gray contours indicate the 68%, 90%, and 99% ranges of the simulation results where the typical parameters and the exposure time were assumed.

Anders & Grevesse (1989), in which the oxygen abundance was 41% higher than that shown in Lodders et al. (2009). The oxygen abundance directly affects the flux (and therefore EM_{halo}) of the hot gaseous halo model because emissions from oxygen, including the radiative recombination continua, dominate the 0.4–1.0 keV flux of a hot gas with $kT \sim 0.26$ keV. Third is the difference in the AtomDB versions. The emissivities of the Fe L-shell lines in the 0.7–0.9 keV band for AtomDB 1.3.1 were $\sim$60% lower than those for AtomDB 3.0.9. That leads to higher iron abundances in Y09 compared to our results. Fourth is the treatment of the neon abundance. The free neon abundance has

a slight effect on kT_{halo} and EM_{halo}. When we reanalyzed our data with the same settings as Y09 for the above four points, we obtained the results consistent with those of Y09. We also confirmed that the differences in the CXB model and the absorption column density hardly affect the results.

The parameter differences between this study and Y09's study are not considered to be systematic uncertainties for the following reasons. First, there is no incentive to fix EM_{local} to a certain value, considering the one order of magnitude flux variation in the local component found by other observations (e.g., Henley & Shelton 2015; Liu et al. 2017). Second, using
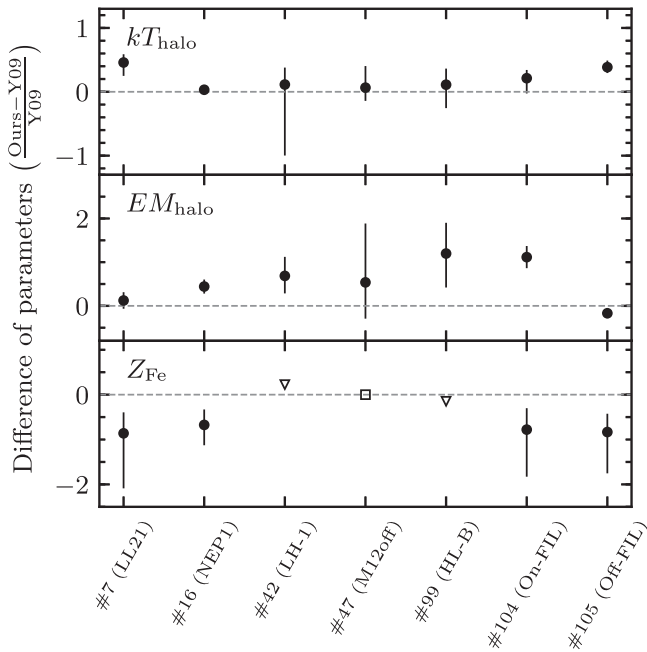
Figure 9. Comparison of the best-fit parameters between our results and those of Y09 for the same observations. The region numbers in this paper are shown on the horizontal axis with the corresponding region names in Y09. Statistical errors from the two results are added quadratically. The downward-pointing triangles indicate the upper limits. The square indicates that the parameter is fixed in both this study and Y09.

an up-to-date database of the solar abundance and the atomic database provides the current best estimates of the parameters. In particular, the emissivities of the strong Fe L-shell lines have been calibrated with grating spectrometer observations over the past decade. Third, fixing the neon abundance to the same solar value as for the oxygen abundance is physically motivated as both neon and oxygen are primarily synthesized by core-collapse supernovae, and therefore they are likely to have the same abundance relative to the solar values. Indeed, the abundances of oxygen and neon relative to the solar values are consistent with each other in the intracluster medium (e.g., Mernier et al. 2016).

4.1.2. Previous XMM-Newton Results

Henley & Shelton (2013, hereafter HS13) analyzed 110 lines of sight out of the Galactic plane ($|b| > 30°$) using the *XMM-Newton* observations. They derived temperatures and emission measures from the 0.4–5.0 keV spectral modeling assuming solar metallicity for the hot gas.

We compared kT_{halo} and EM_{halo} from our study with those of HS13 (Figure 10). In this plot, we only show the data at $75° < l < 285°$ and $|b| > 30°$, areas that both this study and HS13 analyzed. The scatter plot shows a similar trend between the two. However, the median temperature from our result is ~ 0.1 keV higher than that of HS13, and the median emission measure from our result is $\sim 50\%$ higher than that of HS13.

The shift in the median kT_{halo} is likely due to the differences in EM_{local}. We allowed EM_{local} to vary, while HS13 fixed EM_{local} according to the count rates of the *ROSAT* R12 band obtained from the shadowing observations of nearby dark clouds (Snowden et al. 2000) because it is difficult to determine EM_{local} from the *XMM-Newton* spectrum itself owing to the heavy contamination of the soft proton background below

1 keV. The median *ROSAT* count rate in the HS13 analysis is ~ 600 counts s^{-1} arcmin^{-1}. Assuming a temperature of 0.1 keV and solar metallicity, this count rate can be converted to an EM_{local} of $\sim 4 \times 10^{-3}$ cm^{-6} pc, which is lower than our median value of 15×10^{-3} cm^{-6} pc by a factor of ~ 4. Lower EM_{local} leads to lower kT_{halo} as shown by the contours in the right panel of Figure 8; if we fix EM_{local} to 4×10^{-3} cm^{-6} pc, the median kT_{halo} decreases to 0.18 keV and becomes consistent with that of HS13, but the fitting statistics become considerably worse. The result indicates that the extrapolation of the *ROSAT* R12 band (0.11–0.28 keV) flux to the analysis energy band (0.4–5.0 keV) has systematic uncertainties due to the different contributions of the SWCX emission between those two bands and/or the different solar activity between the *ROSAT* era and the *Suzaku/XMM-Newton* era.

The shift in the median EM_{halo} is caused by the difference in the solar abundance. As shown in the case of Y09, HS13 used the solar abundance of Anders & Grevesse (1989). The 41% higher oxygen abundance in Anders & Grevesse (1989) compared to that in Lodders et al. (2009) increases the flux of the hot gaseous halo model by $\sim 40\%$. This explains the difference in EM_{halo} between our results and those of H13.

4.2. Contamination of Unresolved Stellar Sources

Kuntz & Snowden (2001) estimated the contribution of unresolved stellar sources to the soft X-ray background flux measured with *ROSAT* and concluded that it is negligible at least for $|b| > 30°$. Yoshino et al. (2009) calculated the flux of unresolved dM stars assuming the stellar distribution model and found that the integrated flux is lower than the observed flux by a factor of 5. Even though minor contributions of stellar sources to the soft X-ray background were shown in previous studies, we reevaluated the possible contamination of stellar sources at low Galactic latitudes using recent observations of stellar sources.

According to the log N–log S plot of active coronae reported by Nebot Gómez-Morán et al. (2013), the integrated surface brightness of the unresolved stars below a flux of 5×10^{-14} erg cm^{-2} s^{-1} is $\sim 0.5 \times 10^{-12}$ erg cm^{-2} s^{-1} deg^{-2}. That is <20% of the surface brightness of the hot gaseous halo at $15° < |b| < 20°$. Therefore, the contribution of unresolved stellar sources to the observed flux is not significant.

4.3. Spatial Distribution of the Hot Gas

Two types of density distribution models for the hot gaseous halo have been proposed. One is a disk-like morphology suggested by the combined analysis of emission- and absorption-line measurements (e.g., Yao et al. 2009). The other is a spherical distribution model, in particular, the modified β-model constructed by Miller & Bregman (2013, 2015). We compared these two models with our emission measure data.

Spatial correlations between EM_{halo} and the Galactic coordinates are key to distinguishing the models. The disk-like morphology predicts that EM_{halo} is proportional to $\csc|b|$ ($=1/\sin|b|$). Conversely, the spherical distribution model predicts decreasing EM_{halo} with increasing angle from the Galactic center ($\theta = \arccos(\cos l \cos b)$). We examined these points in Figure 11. The binned data (red crosses) are also shown in the figure to smooth out the large scatter of the data points. A positive correlation is shown in the left panel

Table 3
Fitting Results of the Density Distribution Models

Model	Parameters of the Disk Model			Parameters of the Spherical Model		
	n_0 (10^{-3} cm^{-3})	R_0 (kpc)	z_0 (kpc)	n_c (10^{-3} cm^{-3})	r_c (kpc)	β
EM$_{\rm disk}$	$3.8^{+2.2}_{-1.2}$	$7.0^{+2.1}_{-1.7}$	$2.7^{+0.8}_{-0.7}$	...	...	...
EM$_{\rm sphe}$	...	...	...	$4.3^{+0.1}_{-0.1}$	2.4 (fixed)	0.51 (fixed)
EM$_{\rm disk+sphe}$	$3.7^{+0.4}_{-0.4}$	7.0 (fixed)	$1.8^{+0.7}_{-0.8}$	$1.2^{+0.8}_{-0.8}$	2.4 (fixed)	0.51 (fixed)

Note. Uncertainties are the 16th to 84th percentile ranges of the posterior distributions.
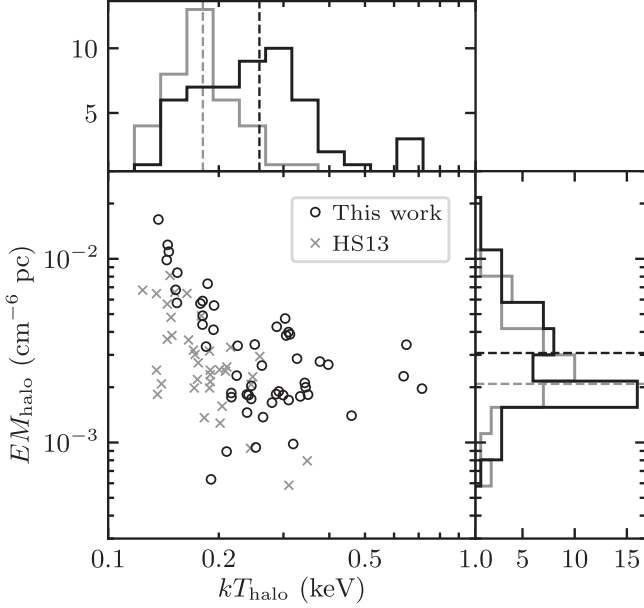
Figure 10. Scatter plot of EM$_{\rm halo}$ vs. $kT_{\rm halo}$ for this study (black) and those of H13 (gray). We only show the data at $75° < l < 285°$ and $|b| > 30°$ to match the analyzed sky regions. Error bars are not shown to simplify the plot. The histograms on the top and right sides of the scatter plot are the distributions of $kT_{\rm halo}$ and EM$_{\rm halo}$, respectively, with the median shown by the dashed lines.

(EM$_{\rm halo}$–csc$|b|$ plot), whereas no clear correlation is shown in the right panel (EM$_{\rm halo}$–θ plot). Therefore, a disk-like morphology is qualitatively favored.

To perform quantitative analyses, we formulated the models as follows. According to Li & Bregman (2017), the disk model ($n_{\rm disk}$) is parameterized by the scale length (R_0) and the scale height (z_0) such that

$$n_{\rm disk}(R, z) = n_0 \exp\left(-\frac{R}{R_0}\right)\exp\left(-\frac{z}{z_0}\right), \quad (2)$$

where R is the distance from the Galactic center projected onto the Galactic plane, z is the vertical height from the Galactic plane, and n_0 is the normalization factor corresponding to the number density at the Galactic center. The spherical distribution model (modified β model) used by Miller & Bregman (2015) is described as

$$n_{\rm sphe}(r) = n_c\left(\frac{r}{r_c}\right)^{-3\beta}, \quad (3)$$

where $n_{\rm sphe}$ is the number density, r is the distance from the Galactic center, n_c is the core density, r_c is the core radius, and β is the slope of the profile. Assuming a line-of-sight distance from the Sun (s), R, z, and r are described as a function of the

Galactic coordinates:

$$R(l, b, s) = \sqrt{D_\odot^2 + (s \cos b)^2 - 2D_\odot s \cos b \cos l}, \quad (4)$$

$$z(b, s) = s \sin b, \quad (5)$$

$$r(l, b, s) = \sqrt{R(l, b, s)^2 + z(l, b, s)^2}, \quad (6)$$

where $D_\odot$ is the distance between the Sun and the Galactic center (8 kpc). We then derive the emission measures predicted by these density models at a certain line of sight as

$$\mathrm{EM}_{\rm disk}(l, b) = \int_0^{s_{\rm max}} n_{\rm disk}^2(R(l, b, s), z(b, s))ds, \quad (7)$$

$$\mathrm{EM}_{\rm sphe}(l, b) = \int_0^{s_{\rm max}} n_{\rm sphe}^2(r(l, b, s))ds, \quad (8)$$

where $s_{\rm max}$ is the maximum path length of the integration. We assumed an $s_{\rm max}$ of 100 kpc in the following discussion. Values of $s_{\rm max}$ larger than 100 kpc did not affect the results.

First, we fitted the EM$_{\rm disk}$ model to the data using the Markov chain Monte Carlo (MCMC) package emcee (Foreman-Mackey et al. 2013). The maximum likelihood estimator was constructed from the χ^2 values. We ran 10^7 steps with an ensemble of 100 walkers. We confirmed that the autocorrelation times of each parameter were shorter than the step numbers by a factor of >10. Posterior distributions were constructed from the last 10^5 steps (hence 10^7 samples). Figure 12 shows the resulting posterior distribution of the EM$_{\rm disk}$ model. The medians of the parameters are shown in Table 3. The quoted uncertainties are the 16th to 84th percentiles. The dashed curves in Figure 13 show representatives of the EM$_{\rm disk}$ model at $|l| = 90°$, $120°$, $150°$, and $180°$. Observed emission measures in the corresponding $|l|$ ranges are also shown by the gray points. The model approximates the observed data even though a large scatter ($\approx$40%) of the data around the model is present. To smooth out the possible intrinsic scatter of the data, we also show the binned data in Figure 13 with the red crosses. The binned data roughly agree with the EM$_{\rm disk}$ model. The obtained n_0 and z_0 are consistent with those derived from previous studies toward LMC X-3, PKS 2155−204, and Mrk 421, where $n_0 = (1–5) \times 10^{-3}$ cm^{-3} and $z_0 = 2–9$ kpc (Yao et al. 2009; Hagihara et al. 2010; Sakai et al. 2014).

Then, we fitted the EM$_{\rm sphe}$ model in the same manner as the above EM$_{\rm disk}$ fitting. Because r_c and β were not well constrained in our fitting, we fixed them to 2.4 kpc and 0.51, respectively, according to the results of Li & Bregman (2017). The fitted parameters are shown in Table 3, and the representative mode curves (dot-dashed curves) are shown in Figure 13. In contrast to the EM$_{\rm disk}$ model, the EM$_{\rm sphe}$ model increases with increasing $|b|$ and therefore is not in line with the tendency of the data, especially at $75° < |l| < 105°$ and $105° < |l| < 135°$. The obtained n_c is consistent with the value
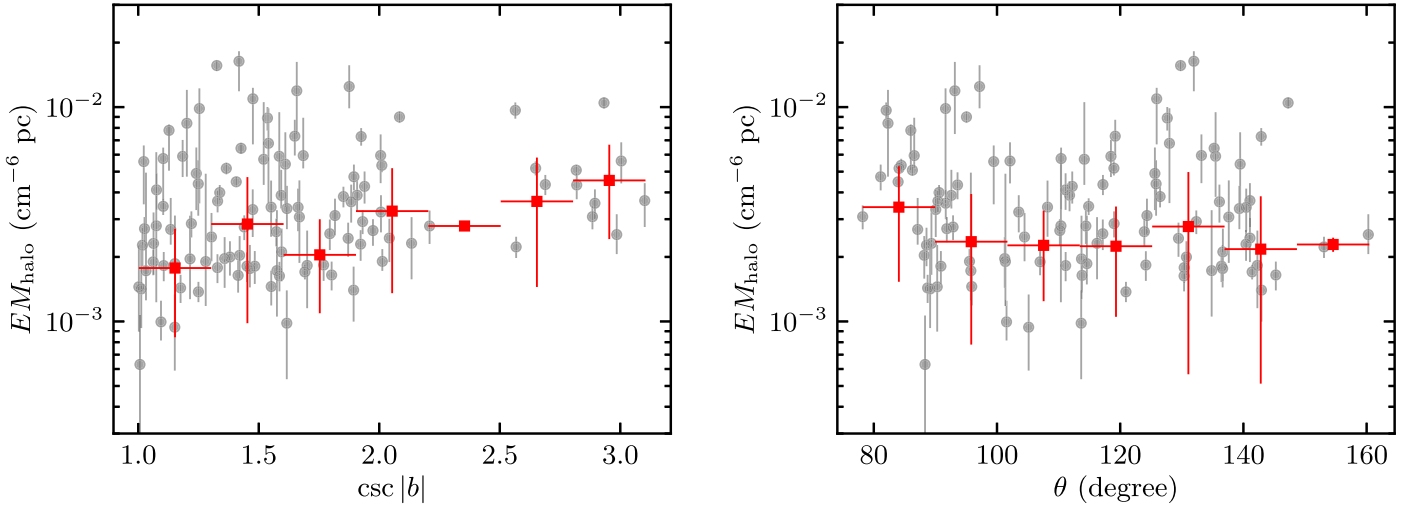
Figure 11. Emission measures of the hot gaseous halo component along $\csc|b|$ (left) and $\theta = \arccos(\cos l \cos b)$ (right). The gray data points are the emission measures for individual *Suzaku* lines of sight, whereas the red data points are the inverse squared-error weighted means calculated from the intervals shown in the horizontal red bars. The vertical red bars indicate the corresponding inverse squared-error weighted standard deviations.
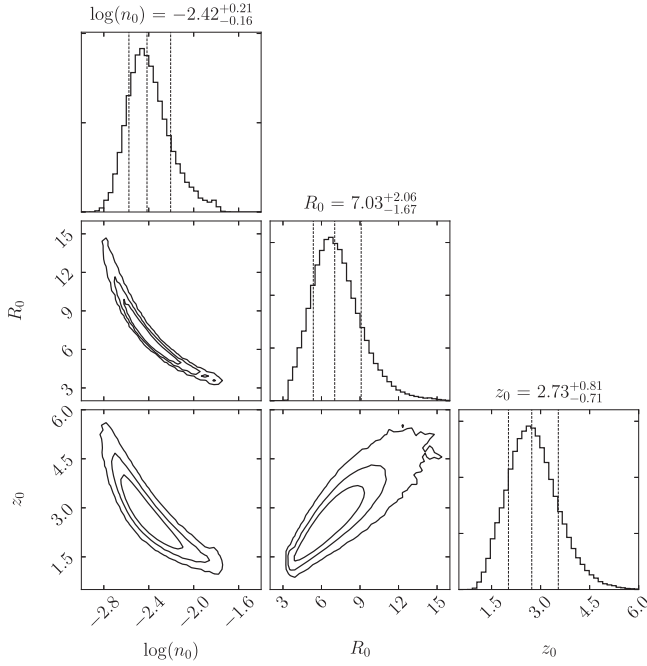

Figure 12. Posterior probability distributions of the disk model parameters derived from the fitting with the MCMC simulations. The vertical dotted lines of each histogram indicate the 16th, 50th, and 84th percentiles. Contours indicate the 68%, 90%, and 99% levels.

shown in Miller & Bregman (2015) and is approximately half of that in Li & Bregman (2017).

Finally, we constructed a composite of the disk and the spherical models where the density and the emission measure are described as

$$n_{\mathrm{disk+sphe}} = n_{\mathrm{disk}} + n_{\mathrm{sphe}} \tag{9}$$

and

$$\mathrm{EM}_{\mathrm{disk+sphe}} = \int_0^{s_{\max}} n_{\mathrm{disk+sphe}}^2 ds, \tag{10}$$

respectively. In this composite model, we fixed r_c and β as in the fitting of the $\mathrm{EM}_{\mathrm{sphe}}$ model. In addition, R_0 was fixed to

7.0 kpc, which was obtained from the $\mathrm{EM}_{\mathrm{disk}}$ model fitting, because this parameter was not well constrained in the composite model fitting. The fitting with the MCMC simulation gives the posterior distributions shown in Figure 14 and the parameter ranges summarized in Table 3. The fitted parameters of the disk model component are consistent with those obtained from the $\mathrm{EM}_{\mathrm{disk}}$ model fitting, while the normalization of the spherical model component is lower than that obtained from the $\mathrm{EM}_{\mathrm{sphe}}$ model fitting by a factor of ~ 4. The blue curves in Figure 13 are representatives of the $\mathrm{EM}_{\mathrm{disk+sphe}}$ model at $|l| = 90°$, $120°$, $150°$, and $180°$. As shown in this figure, the $\mathrm{EM}_{\mathrm{disk+sphe}}$ model is nearly the same as the $\mathrm{EM}_{\mathrm{disk}}$ model, and the contribution of the spherical model component is minor.

A similar composite model was also examined by Li & Bregman (2017) using the emission-line data of *XMM-Newton*. For comparison, we calculated the model densities at the solar neighborhood; $n_{\mathrm{disk},\odot}$ was calculated from the disk model at $R = 8$ kpc and $z = 0$ kpc, and $n_{\mathrm{sphe},\odot}$ was calculated from the spherical model at $r = 8$ kpc. These values are shown in Table 4. Both results indicate that the density of the disk model is higher than that of the spherical model in the solar neighborhood. The quantitative difference likely reflects systematic uncertainties between the different analysis methods. For example, Li & Bregman (2017) assumed a constant temperature of 2×10^6 K; however, our spectroscopic results show that the median temperature is 3×10^6 K with $\sim 30\%$ fluctuations.

The fitting with our composite model suggests that the observed X-ray emissions primarily originate in the disk component rather than in the spherical component. However, the contribution to the mass of the gaseous halo has the opposite trend. The total mass of the disk model component is

$$
\begin{aligned}
M_{\mathrm{disk}} &= \int_0^{z_{\max}} \int_0^{R_{\max}} \frac{\mu m_p n_{\mathrm{disk}}(R, z)}{Z} 2\pi R \, dR \, dz \\
&= 5 \times 10^7 \left(\frac{Z}{Z_\odot}\right)^{-1} M_\odot, \tag{11}
\end{aligned}
$$

where μ is the mean atomic weight of 0.61, m_p is the proton mass, Z is the metallicity of the gas, and both $R_{\max}$ and $z_{\max}$ are
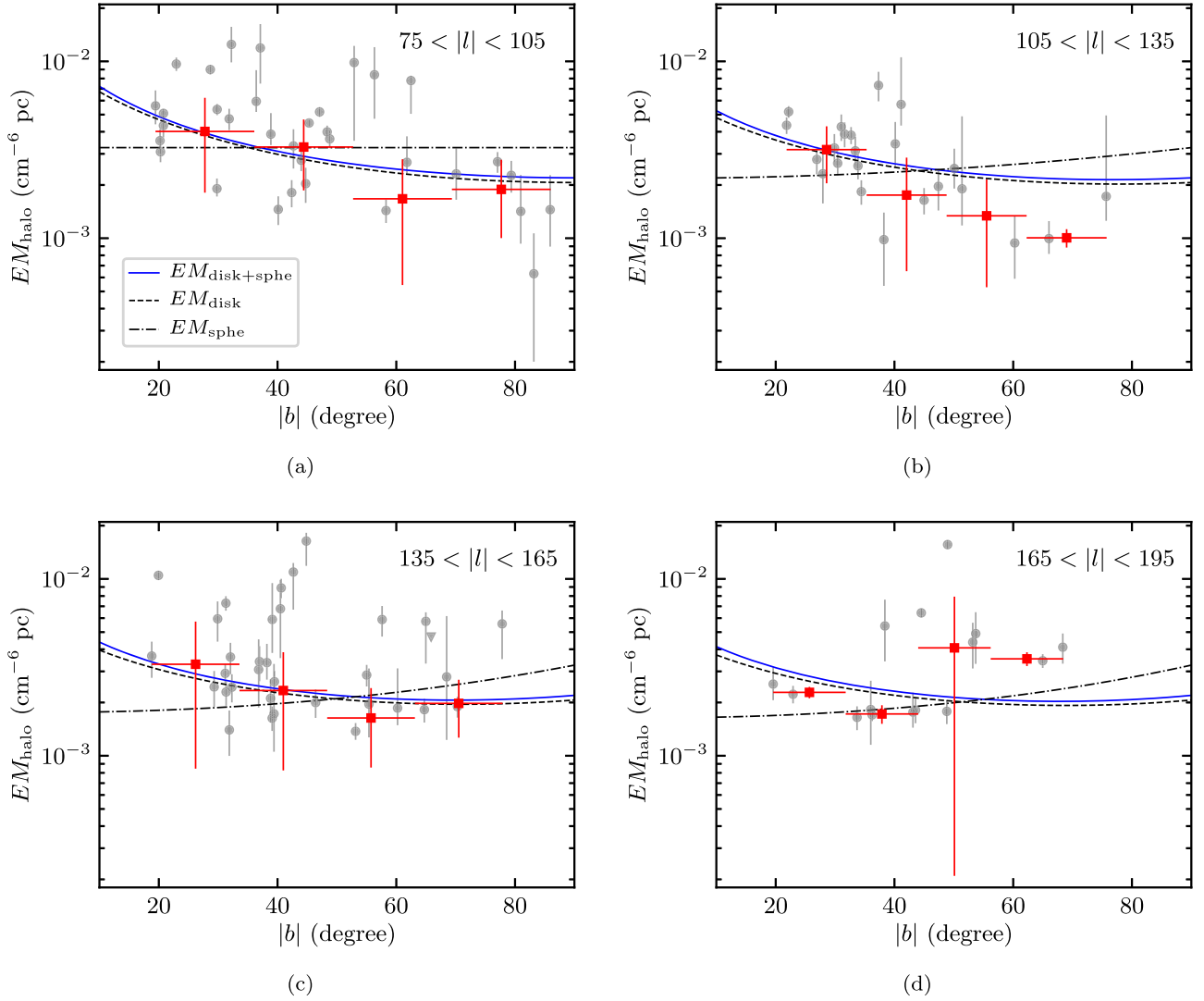
Figure 13. Emission measures of the hot gaseous halo vs. the absolute value of the Galactic latitude. Each panel shows a different range of the Galactic longitude: (a) $|l| = 90° \pm 15°$, (b) $|l| = 120° \pm 15°$, (c) $|l| = 150° \pm 15°$, and (d) $|l| = 180° \pm 15°$. The fitted disk and spherical models are shown by the dashed and dot-dashed curves, respectively, and the solid (uppermost) lines are their composite. The red data points are the inverse squared-error weighted means calculated from the intervals shown by the horizontal bars, with weighted standard deviations shown by the vertical bars.

assumed to be 30 kpc. Larger R_{max} and z_{max} do not affect the resulting mass. On the other hand, the total mass of the spherical model component is described as

$$M_{sphe} = \int_0^{r_{max}} \frac{\mu m_p n_{sphe}(r)}{Z} 4\pi r^2 dr$$
$$= 2 \times 10^9 \left(\frac{Z}{Z_\odot}\right)^{-1} M_\odot, \qquad (12)$$

where r_{max} is assumed to be 250 kpc, which is the viral radius of our Galaxy. As shown in Figure 15, even when r_{max} is ~30 kpc, M_{sphe} is comparable to M_{disk}. Note that the extended spherical hot gas cannot explain the missing baryons in the MW (~$10^{11} M_\odot$), even taking into account a low metallicity of $Z \sim 0.3 Z_\odot$.

The smaller contribution of the spherical component to the X-ray emissions, despite its significant mass contribution, is caused by its low density because the X-ray flux of the diffuse hot gas is $\propto n^2$ and is biased toward high-density regions. To constrain the parameters of the spherical component, a large number of samples of absorption-line measurements are necessary.

4.4. Origin of the Hot Gaseous Halo

Our X-ray emission data reveal the existence of a disk-like hot gas. However, a more extended hot gas region is proposed by other indirect observations such as the pressure confinement of high-velocity clouds in the MW halo (e.g., Fox et al. 2005) and the ram pressure stripping of local dwarf galaxies (e.g., Grcevich & Putman 2009). Therefore, we consider that the hot gaseous halo consists of a disk-like component and an extended spherical component.

A hot gas with a disk-like morphology is expected from stellar feedback in the MW disk; this is the so-called Galactic fountain model (e.g., Shapiro & Field 1976; Norman & Ikeuchi 1989). The scale height we obtained (~2 kpc) is much smaller than that calculated from the assumption of hydrostatic equilibrium between the Galactic gravitational potential and the pressure gradient of a hot gas with a constant temperature of 0.26 keV (10–20 kpc). This indicates that the disk-like hot gas
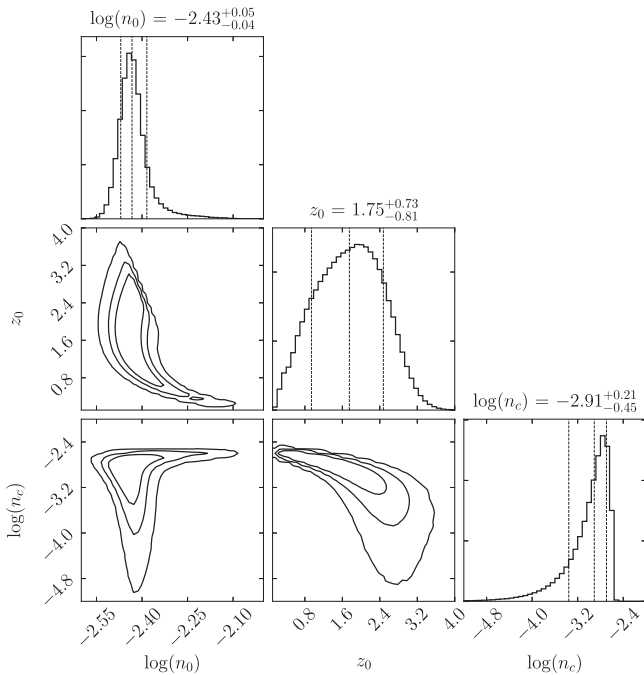
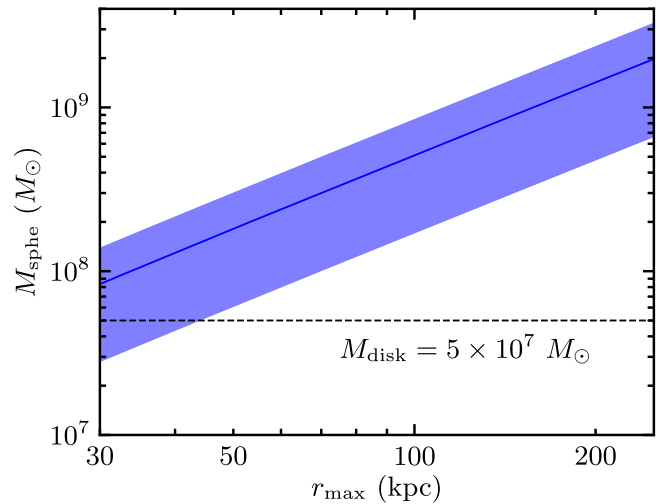**Figure 14.** Same as Figure 12, but for the $EM_{disk+sphe}$ model.

Figure 15. Integrated mass of the spherical component as a function of the assumed r_{max}. The blue hatched area shows the uncertainty obtained from the fitting. The estimated M_{disk} is shown as the horizontal dashed line. Solar metallicity is assumed for both M_{sphe} and M_{disk}.

Table 4
Model Densities in the Solar Neighborhood

Model	$n_{disk,\odot}$[a] $(10^{-3}\,cm^{-3})$	$n_{sphe,\odot}$[b] $(10^{-3}\,cm^{-3})$	$\frac{n_{disk,\odot}}{n_{sphe,\odot}}$
This work	1.2	0.2	6.1
Li & Bregman (2017)	2.5	1.2	2.1

Notes.
[a] Density of the disk component at $R = 8$ kpc and $z = 0$ kpc.
[b] Density of the spherical component at $r = 8$ kpc.

is not in hydrostatic equilibrium. Indeed, numerical simulations of stellar feedback show a steep gradient of the hot gas density at $z \lesssim 1$ kpc, which is the launching site of hot gases generated by multiple supernovae in the galactic disk (Hill et al. 2012; Kim & Ostriker 2018). The large scatter of the EM_{halo} around the model is also naturally explained by the stellar feedback model.

One problem with the stellar feedback model is that it underpredicts the hot gas density (and therefore the X-ray flux) as reported by Henley et al. (2015b). As pointed out by the authors, considering a spherically distributed hot gas and/or other driving mechanisms such as cosmic-ray-driven outflows would mitigate the discrepancy between the observations and the numerical simulations.

4.5. The Metal Abundance of the Hot Gaseous Halo

For the first time, we derived a median $[O/Fe]_{halo}$ of 0.25 using 46 lines of sight. Even though this is subject to future updates of the atomic database and/or high-resolution spectroscopy that resolves the Fe L-shell lines, this value is currently the best estimate with the latest databases.

The abundance ratio of $[O/Fe]_{halo}$ provides complementary information concerning the origin of the hot gaseous halo. Recent systematic observations of clusters of galaxies show that the ratio of α-elements to Fe is consistent with the solar value in the

intracluster medium (Matsushita et al. 2007; Mernier et al. 2016). This trend holds even at cluster outskirts, where the metallicity is as low as $\sim$0.2 $Z_\odot$ (Simionescu et al. 2015). Therefore, the intergalactic medium probably has [O/Fe] abundance ratio of the solar value. On the other hand, chemical composition of the outflowing hot gas from the MW disk reflects the recent rate of core-collapse supernovae (SN_{cc}) to Type Ia supernova (SN_{Ia}) in the MW because the cooling time of the hot gas is $\approx$1 Gyr. Because the estimated SN_{cc}-to-SN_{Ia} rate for the recent MW is $\approx$5 (Li et al. 2011), [O/Fe] is expected to be $\sim$0.17 according to metal yields of SN_{cc} and SN_{Ia} described in Kobayashi et al. (2006). The observed [O/Fe] roughly agrees with the above simple estimation, even though the actual abundance ratio is also affected by the mass-loading factor, which is highly uncertain. Therefore, it supports the stellar feedback scenario for the X-ray-emitting hot gas rather than accretion from the intergalactic medium.

4.6. High-temperature Regions

We found six lines of sight (22, 53, 70, 72, 75, and 94) that have temperatures of $>$0.4 keV, which is higher than the typical temperature range of 0.19–0.32 keV (Figure 5). These high-temperature regions are not concentrated in a specific sky region but are distributed randomly (Figure 4). Such a high-temperature region was also reported by Henley & Shelton (2013) at $(l, b) = (237°.924, -54°.594)$.

The origin of these high-temperature regions is still unclear. However, spatial fluctuations in the temperature are natural if the stellar feedback scenario is correct. Indeed, the observed temperature range is consistent with the typical temperature range of middle-aged Galactic supernova remnants. Therefore, the high-temperature regions might reflect fresh hot gases outflowing from the MW disk. Another possibility is extragalactic hot gas associated with galaxy filaments (Mitsuishi et al. 2014). Further observations covering large fractions of the blank X-ray sky are necessary to further examine the origins of these regions.

5. Conclusions

We derived the properties of the MW hot gaseous halo from an X-ray spectral analysis of 107 lines of sight from the *Suzaku*

observations at $75° < l < 295°$ and $|b| > 15°$. The spectral model in the 0.4–5.0 keV band consists of three components: the hot gaseous halo component represented by a single-temperature CIE plasma, the local emission component empirically mimicked by a single-temperature CIE plasma, and the CXB component with a single power-law function. We used the latest atomic database and solar abundance table, which affect the emission measure and the iron abundance.

The median temperature in the observed fields is 0.26 keV $(3.0 \times 10^6$ K), and the 16th–84th percentile range is 0.19–0.32 keV $((2.2–3.8) \times 10^6$ K), showing a $\sim$30% spatial fluctuation in the temperature. The derived emission measure ranges over $(0.6–16.4) \times 10^{-3}$ cm^{-6} pc. We also constrained [O/Fe]$_{halo}$ for the 46 lines of sight, and its median is 0.25. The emission measure marginally correlates with csc $|b|$.

The spatial distribution of EM$_{halo}$ is approximated by a disk-like density distribution with $n_0 \sim 4 \times 10^{-3}$ cm^{-3}, $R_0 \sim 7$ kpc, and $z_0 \sim 2$ kpc, even though there is a $\sim$40% scatter of the data around the model. We also found that the contribution of the extended spherical hot gas to the observed X-ray emission is minor but its mass contribution is much higher than that of the disk-like component. This is because the X-ray flux, which is proportional to the square of the density, is biased toward high-density regions.

The disk-like hot gas component likely results from stellar feedback in the MW disk, according to its small scale height and the large scatter of EM$_{halo}$. The over-solar [O/Fe]$_{halo}$ indicates a significant contribution of core-collapse supernovae and supports the stellar feedback scenario.

In addition, we found six lines of sight that have significantly high temperatures ($>$0.4 keV). The possible origin of these high-temperature regions is hot gas recently outflowing from the MW disk and/or extragalactic hot gas filaments between galaxies.

Software: Astropy (Astropy Collaboration et al. 2013), APEC (Foster et al. 2012), CIAO (Fruscione et al. 2006), corner.py (Foreman-Mackey 2016), emcee (Foreman-Mackey et al. 2013), HEAsoft (v6.22; Arnaud 1996), Matplotlib (Hunter 2007), TBabs (v2.3; Wilms et al. 2000), xisnxbgen (Tawa et al. 2008), xisrmfgen and xissimarfgen (Ishisaki et al. 2007).

ORCID iDs

Shinya Nakashima https://orcid.org/0000-0002-7808-8693
Yoshiyuki Inoue https://orcid.org/0000-0002-7272-1136
Yoshiaki Sofue https://orcid.org/0000-0002-4268-6499
Jun Kataoka https://orcid.org/0000-0003-2819-6415

References

Anders, E., & Grevesse, N. 1989, GeCoA, 53, 197
Arnaud, K. A. 1996, in ASP Conf. Ser. 101, Astronomical Data Analysis Software and Systems V, ed. G. H. Jacoby & J. Barnes (San Francisco, CA: ASP), 17
Astropy Collaboration, Robitaille, T. P., Tollerud, E. J., et al. 2013, A&A, 558, A33
Cappelluti, N., Li, Y., Ricarte, A., et al. 2017, ApJ, 837, 19
Cash, W. 1979, ApJ, 228, 939
Crain, R. A., McCarthy, I. G., Frenk, C. S., Theuns, T., & Schaye, J. 2010, MNRAS, 407, 1403
Dickey, J. M., & Lockman, F. J. 1990, ARA&A, 28, 215
Fang, T., Marshall, H. L., Lee, J. C., Davis, D. S., & Canizares, C. R. 2002, ApJL, 572, L127
Foreman-Mackey, D. 2016, JOSS, 1, 24
Foreman-Mackey, D., Hogg, D. W., Lang, D., & Goodman, J. 2013, PASP, 125, 306
Foster, A. R., Ji, L., Smith, R. K., & Brickhouse, N. S. 2012, ApJ, 756, 128
Fox, A. J., Wakker, B. P., Savage, B. D., et al. 2005, ApJ, 630, 332
Fruscione, A., McDowell, J. C., Allen, G. E., et al. 2006, Proc. SPIE, 6270, 62701V
Fujimoto, R., Mitsuda, K., Mccammon, D., et al. 2007, PASJ, 59, 133
Galeazzi, M., Gupta, A., Covey, K., & Ursino, E. 2007, ApJ, 658, 1081
Grcevich, J., & Putman, M. E. 2009, ApJ, 696, 385
Gupta, A., Mathur, S., Krongold, Y., Nicastro, F., & Galeazzi, M. 2012, ApJL, 756, L8
Hagihara, T., Yao, Y., Yamasaki, N. Y., et al. 2010, PASJ, 62, 723
Henley, D. B., & Shelton, R. L. 2013, ApJ, 773, 92
Henley, D. B., & Shelton, R. L. 2015, ApJ, 808, 22
Henley, D. B., Shelton, R. L., Cumbee, R. S., & Stancil, P. C. 2015a, ApJ, 799, 117
Henley, D. B., Shelton, R. L., & Kuntz, K. D. 2007, ApJ, 661, 304
Henley, D. B., Shelton, R. L., Kwak, K., Hill, A. S., & Mac Low, M.-M. 2015b, ApJ, 800, 102
Hill, A. S., Ryan Joung, M., Mac Low, M.-M., et al. 2012, ApJ, 750, 104
Hunter, J. D. 2007, CSE, 9, 90
Ishikawa, K., Ezoe, Y., Miyoshi, Y., et al. 2013, PASJ, 65, 63
Ishisaki, Y., Maeda, Y., Fujimoto, R., et al. 2007, PASJ, 59, 113
Joung, M. R., Putman, M. E., Bryan, G. L., Fernández, X., & Peek, J. E. G. 2012, ApJ, 759, 137
Kalberla, P. M. W., Burton, W. B., Hartmann, D., et al. 2005, A&A, 440, 775
Kataoka, J., Tahara, M., Totani, T., et al. 2013, ApJ, 779, 57
Kereš, D., Katz, N., Fardal, M., Davé, R., & Weinberg, D. H. 2009, MNRAS, 395, 160
Kim, C.-G., & Ostriker, E. C. 2018, ApJ, 853, 173
Kobayashi, C., Umeda, H., Nomoto, K., Tominaga, N., & Ohkubo, T. 2006, ApJ, 653, 1145
Koyama, K., Tsunemi, H., Dotani, T., et al. 2007, PASJ, 59, 23
Kuntz, K. D., & Snowden, S. L. 2001, ApJ, 554, 684
Li, W., Chornock, R., Leaman, J., et al. 2011, MNRAS, 412, 1473
Li, Y., & Bregman, J. 2017, ApJ, 849, 105
Liu, W., Chiao, M., Collier, M. R., et al. 2017, ApJ, 834, 33
Lodders, K., Palme, H., & Gail, H.-P. 2009, LanB, 4, 712
Matsushita, K., Böhringer, H., Takahashi, I., & Ikebe, Y. 2007, A&A, 462, 953
McCammon, D., Almy, R., Apodaca, E., et al. 2002, ApJ, 576, 188
McCammon, D., & Sanders, W. T. 1990, ARA&A, 28, 657
Mernier, F., de Plaa, J., Pinto, C., et al. 2016, A&A, 595, A126
Miller, M. J., & Bregman, J. N. 2013, ApJ, 770, 118
Miller, M. J., & Bregman, J. N. 2015, ApJ, 800, 14
Miller, M. J., & Bregman, J. N. 2016, ApJ, 829, 9
Mitsuda, K., Bautz, M., Inoue, H., et al. 2007, PASJ, 59, S1
Mitsuishi, I., Kawahara, H., Sekiya, N., et al. 2014, ApJ, 783, 137
Moretti, A., Pagani, C., Cusumano, G., et al. 2009, A&A, 493, 501
Nakashima, S., Nobukawa, M., Uchida, H., et al. 2013, ApJ, 773, 20
Nebot Gómez-Morán, A., Motch, C., Barcons, X., et al. 2013, A&A, 553, A12
Norman, C. A., & Ikeuchi, S. 1989, ApJ, 345, 372
Sakai, K., Yao, Y., Mitsuda, K., et al. 2014, PASJ, 66, 83
Sekiya, N., Yamasaki, N. Y., Mitsuda, K., & Takei, Y. 2014, PASJ, 66, L3
Serlemitsos, P. J., Soong, Y., Chan, K.-W., et al. 2007, PASJ, 59, S9
Shapiro, P. R., & Field, G. B. 1976, ApJ, 205, 762
Simionescu, A., Werner, N., Urban, O., et al. 2015, ApJL, 811, L25
Smith, R. K., Bautz, M. W., Edgar, R. J., et al. 2007, PASJ, 59, 141
Snowden, S. L., Egger, R., Freyberg, M. J., et al. 1997, ApJ, 485, 125
Snowden, S. L., Freyberg, M. J., Kuntz, K. D., & Sanders, W. T. 2000, ApJS, 128, 171
Stewart, K. R., Maller, A. H., Oñorbe, J., et al. 2017, ApJ, 843, 47
Su, M., Slatyer, T. R., & Finkbeiner, D. P. 2010, ApJ, 724, 1044

Tanaka, Y., & Bleeker, J. A. M. 1977, SSRv, 20, 815
Tawa, N., Hayashida, K., Nagai, M., et al. 2008, PASJ, 60, S11
Tsujimoto, M., Guainazzi, M., Plucinsky, P. P., et al. 2011, A&A, 525, A25
Tumlinson, J., Peeples, M. S., & Werk, J. K. 2017, ARA&A, 55, 389
Ursino, E., Galeazzi, M., & Liu, W. 2016, ApJ, 816, 33

Willingale, R., Starling, R. L. C., Beardmore, A. P., Tanvir, N. R., &
   O'Brien, P. T. 2013, MNRAS, 431, 394
Wilms, J., Allen, A., & McCray, R. 2000, ApJ, 542, 914
Yao, Y., Wang, Q. D., Hagihara, T., et al. 2009, ApJ, 690, 143
Yoshino, T., Mitsuda, K., Yamasaki, N. Y., et al. 2009, PASJ, 61, 805